MEMS-BASED SPATIAL LIGHT MODULATION FOR LONG TERM AND INFRARED BEAM STEERING APPLICATIONS

by

Jiafan Guan

A Thesis Submitted to the Faculty of the

JAMES C. WYANT COLLEGE OF OPTICAL SCIENCES

In Partial Fulfillment of the Requirements

For the Degree of

MASTER OF SCIENCE

In the Graduate College

THE UNIVERSITY OF ARIZONA

2021

THE UNIVERSITY OF ARIZONA
GRADUATE COLLEGE

As members of the Master's Committee, we certify that we have read the thesis prepared by **Jiafan Guan**, titled ***MEMS-Based Spatial Modulation for Long Term and Infrared Beam Steering Applications*** and recommend that it be accepted as fulfilling the thesis requirement for the Master's Degree.

Yuzuru Takashima
Professor Yuzuru Takashima Date: May 13, 2021

Professor James T. Schwiegerling Date: 5/13/21

Professor Daewook Kim Date: 5/13/21

Final approval and acceptance of this thesis is contingent upon the candidate's submission of the final copies of the thesis to the Graduate College.

I hereby certify that I have read this thesis prepared under my direction and recommend that it be accepted as fulfilling the Master's requirement.

Yuzuru Takashima
Professor Yuzuru Takashima Date: May 13, 2021
Master's Thesis Committee Chair
Wyant College of Optical Sciences

ACKNOWLEDGEMENTS

Here I would like to express my great gratitude to everyone who helped me in my master's career. Whether in life, study, or research. It is with their help that I become what I am now.

First and foremost, I would like to express my most profound respect and gratitude to my Sensei, Dr. Yuzuru Takashima. A rigorous, patient, conscientious, responsible, and creative professor. His careful guidance helped me develop good research habits in the past two years and developed my rigorous logical thinking. When I encountered difficulties and stalled in the experiment, he could always lead me in the right direction and enable me to make rapid and quality progress. It was not easy for me to say that science and engineering can be a lifelong career until the two years' devotion to the experiment and Professor Takashima's help taught me how fruitful research was brewed.

Next, I would like to express my deep appreciation to every teacher who has helped me. Thanks to Professor Masud Mansuripur, whose electromagnetic class laid a solid foundation for my theoretical knowledge of optics. Thanks to Professor Rongguang Liang, I learned a lot of essential knowledge of optical engineering from his class. And they also provided me with a lot of help in the process of my Ph.D. application. Thank you again for your careful guidance. I would also like to thank Professor Daewook Kim. In his experimental class, I learned a lot of basic operations of scientific research, which made my research progress more efficient. Thanks to Professor Jim Schwiegerling, thanks to his 512R class, I laid a good foundation for me in optical mathematics. Mathematics is the foundation of all science. Thank him for his careful guidance and help. I would also like to thank two of them for their help in my Thesis defense. Thanks to Professor Young-Sik Kim, thank him for his excellent advice and help with the experimental equipment in the dual

modulation experiment. There will not be a success of my master's study without the help of any of them.

The same thanks go out to my peers at the University of Arizona. Thanks to Brandon Hellman, Heejoo Choi, Chuan Luo, Ted Lee, Xianyue Deng, Parker Liu, Eric Evan, Eunmo Kang, and Sungling Wang, who give me countless support in my research. Thanks to their experimental advice and practical guidance, my projects can progress more efficiently. Each of my research results has its wisdom and credit. I also want to thank two of my best friends, Jingwei Zhao and Yuanxin Guan. Thanks for their company, to give me the infinite joy of life, so that I have more strength every day to meet the classes and experiments.

Finally, I want to express my great thanks to my family member. Thanks to my parents and grandma, thanks for their support, thank them for supporting me in pursuing my dreams and not constraining my freedom. Thanks to my boyfriend, thank him for his company and understanding, patience and care, love and support. Every achievement I make cannot live without them behind me.

The same thanks go out to everyone who has given me support, but I'm not mentioning it here, and I wouldn't achieve what I have now without their help.

TABLE OF CONTENTS

LIST OF FIGURES

LIST OF TABLES

ABSTRACT

MEMS-based spatial modulation device diffractive beam steering enables an efficient way to manipulate light by spatial multiplexing while keeping large area throw product. Such kind of device has been applied in the various field over the past few years. In this thesis: 1) the long-term performance of a Digital Micromirror Device-based beam steering system is evaluated by monitoring diffraction efficiency over 350 hours, with a 360 Hz repetition rate. Also, diffraction efficiency was monitored while increasing the temperature of the mirror array from 45 to 75 degrees C; 2) a dual modulation method is introduced for optically enhance the diffraction efficiency of a Phase Light Modulator based beam steering system and confirmed enhancement of diffraction efficiency at 1550nm illumination from a PLM device designed for the wavelength of 633nm.

Chapter 1. Introduction to MEMS-Based Spatial Modulation Devices

1.1Digital Micromirror Device (DMD)

Digital Micromirror Device (DMD) was originally invented by Texas Instrument in 1987 originally for digital display applications. Since then, application of DMD beyond display area has been actively researched. Laser beam steering technology is one of those which can be used for light detection and ranging (lidar) systems and advanced display systems [1]. Recently using a DMD for diffractive beam and image steering has been proposed. The operation principle relies on synchronizing micro mirrors' movement with short nanosecond illumination that effectively and optically "freeze" micromirror' s movement during mirror transition. The method also enables simultaneous modulation of amplitude and phase that open-up with novel application areas of DMD beyond the state of the art [3,4].

Digital Micromirror Device, or DMD, is considered as a MOEMS (micro-opto-electromechanical system)-based binary spatial light modulator (SLM), where an array of pixels can flip between an "on" and "off" state by rotating +/- 12° about an axis defined by the diagonal of the mirror. Between the on and off state, there is a dynamic transitional state where micro mirror changes its tilt angle. The transition time of DMD is on the order of micro-seconds with a high refresh rate that can goes up to higher than 4kHz (DLP4500), and over 32kHz (DLP7000). In Fig. 1.1, the pixel arrangement of DLP4500 is schematically depicted. Single pixel has a dimension of 7.637x7.637um with a 960x540 (horizontal by vertical) array. The micro mirrors are positioned in a diamond configuration with a corner-to-corner period of 10.8μm as shown in Fig. 1.1(a).

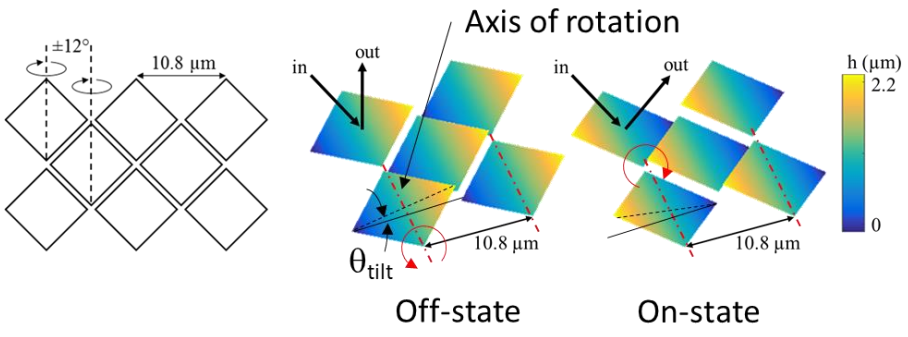

(a) (b)

Figure 1.1 Representation of the (a) 0.45-inch DMD diamond pixel geometry (Top View) with 10.8µm pixel period, mirror can flip between +/- 12°; (b) Schematic of "on" and "off" state of micro mirrors [12] Reprinted with permission from [15] © SPIE.

The unused transitional state of the DMD can be utilized by a short-pulsed laser whose pulse duration is much shorter than the transition time of the mirrors, which enable us to modulate light in a fast manner.

1.1.1 DMD-Based Diffractive Beam Steering

As depicted in last section, DMD can used as a binary spatial light modulator where each of pixels, a micrometer size reflective mirror, tilts in +/- 12 degrees. The incident light is spatially modulated by the tilted mirror. Beam steering in this spatial light modulation mode is feasible, for example by displaying computer generated hologram (CGH) pattern on DMD. Alternatively, DMD at the back focal plane of lens works as a beam steerer by selectively turning on pixels. However, those methods suffer from low photon throughput. Diffraction efficiency of binary amplitude hologram is about 10% [13]. In lens-based beam steering, only a portion of DMD pixels reflects light to lens. Consequently, light throughput defined by the power in the steered beam normalized to the input beam is low. In contrast, the DMD-based diffractive beam steering works as a programmable blazed grating which has an inherently high diffraction efficiency, close to 100% in theory. In

addition, angular throw of beam covers +/- 24° while keeping beam size as large as DMD mirror array area, for example 140mm^2 with a high end DMD device, therefore, etendu (or Lagrange Invariant) of the steering mechanism is kept large [2]. In this manner, a high scan rate, i.e. over 20 kHz, and large Etendu beam steering is feasible while minimizing the number of moving parts [3,4].

The diffraction property of the DMD-based beam steering is governed by the reflection grating equation:

$$m\lambda = d(n\sin\theta + n'\sin\theta') \tag{1}$$

, where m is the order of diffraction, λ is the diffracted wavelength, d is the grating period, n is the illumination side refractive index, n' is the observation side refractive index, θ is the incident angle, and θ' is the diffraction angle as depicted in figure 1.2.

As Eqn. (1) shows the diffraction angle of individual diffraction order depends on several parameters, such as incident wavelength, the blazed angle θ_B of the designed grating, and angle of incidence.

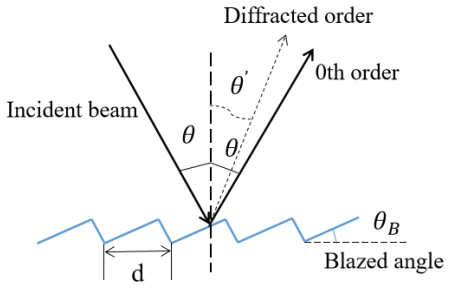

Figure 1.2 Reflection grating diagram.

With the short-pulsed laser, the micromirror movement can be “frozen” at an angle between the stationary “on” and “off” states. Thus, it is feasible to form a programmable blazed diffraction

grating to discretely steer a laser beam with a collimated beam. It is also feasible to create a continuously scanned and diverging beam if the laser beam is focused on a single DMD mirror by eliminating the diffraction grating effects [3].

It is known that the diffraction efficiency depends on the phase profile of reflective grating surface. For a sawtooth blazed grating, it is given by:

$$\eta = sinc^2(1 - \frac{\Delta M}{2}) \quad (2)$$

, where ΔM is the variation of phase modulation of the grating, and η_1 is the diffraction efficiency of +1st diffraction order. In DMD based beam steering, the variable phase profile is implemented in the tilt angle of mirror, or blazed angle. Since the diffraction efficiency depends on the blazed angle of the designed grating, accurate synchronization between the ns laser pulse and mirror transition is needed for this beam steering technique to maximize the diffraction efficiency of discrete beam steering. Figure 1.3 shows a timing diagram for synchronizing ns pulses to DMDs' transitional state. First the mirror transition is initiated by triggering DMD. About 377μs after the external trigger pulse is applied to the DMD driver (Light Crafter 4500, Texas Instruments), mirror starts to transition, and it takes about 3μs to complete the transition. During the 3μs mirror transitional period, laser is triggered. At wavelength of 905nm, and with DLP4500, there are five mirror tilt angles that satisfies a blazed condition. Correspondingly at those timing, input laser is diffracted towards 5 diffraction orders, -2nd, -1st, 0th +1st and +2nd orders.

The refresh rate in this experiment is 360Hz, and the approximated optimized internal time delay for each diffraction order are also listed in Fig. 1.3. We have experimentally verified that two global time delays, 377 and 380.25us exists for this specific model. Every time DMD is hardware

reset, the global delay time changes from one to another value in a repeatable manner. This might be due to ambiguity in initialization logic.

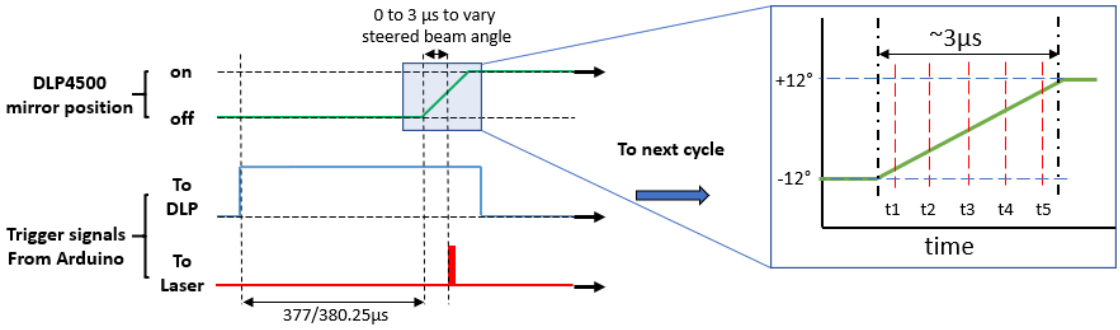

Figure 1.3 Timing diagram of DMD based diffractive beam steering with DLP4500. For global delay 377µs, t_1=0.5µs; t_2=1.25µs; t_3=1.875µs; t_4=2.375µs; t_5=2.75µs. Reprinted with permission from [15] © SPIE.

As an inset of Fig. 1.3, laser synchronization timing is detailed. The timing t_1 to t_5 are additional delays to the global delay for each diffraction order from -2 to +2 order. The optimized internal delay time does not change, while global delay change between 377µs and 380.25µs in a repeatable manner upon restarting the unit.

1.2Phase Light Modulator (PLM)

Texas Instruments PLM (Phase Light Modulator) is a Micro Electromechanical System (MEMS) spatial light modulator that modulates phase of light in a 2-dimensional manner. PLM devices are commonly manufactured by a Liquid Crystal on Silicon (LCoS) processes. PLMs based on the LCoS device process is commercially available, for example from HoloEye, Santec, and Hamamatsu. The drawback in general of such Liquid Crystal (LC) based PLM is slow switching speed in phase modulation. Due to the relatively slow (~ms) response time of LC, applications of

LCoS PLMs are mainly for applications such as displaying images, manipulation of micro particles that do not require a high-speed phase modulation.

In contrast, a faster laser beam modulation is needed for beam steering for light detection and ranging (lidar). Especially a solid state or MEMS (Micro Electromechanical System) based laser beam steering is highly anticipated to replace mechanical scanning modalities such as rotating mirrors and Galvo mirrors. A fast laser beam steering enables a real time recognition of distant object with video frame rate. MEMS based PLMs in general has a faster switching time (~us), compared to the switching time of LC. Such MEMS based PLM operates in a piston mode of electro dynamically controlled array of micromirrors.

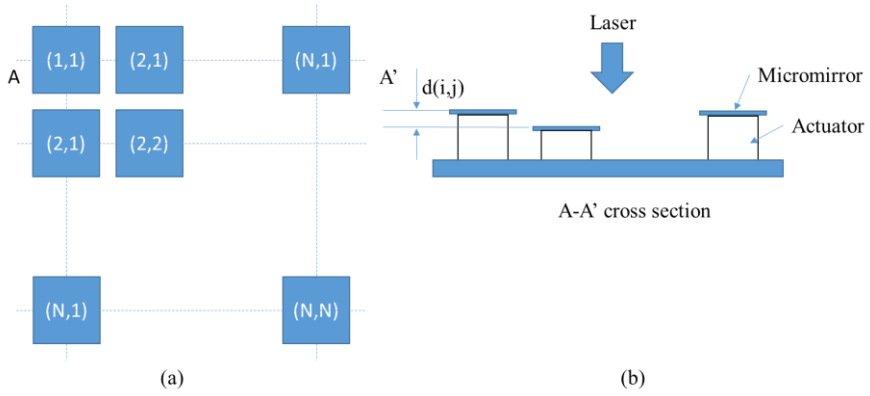

Figure 1.4 Pixel arrangement and micromirrors movement schematic diagram.

Figure 1.4 (a) shows MEMS PLM consists of a pixelated micromirrors that change height of the mirror along the direction of incidence of light. Variation of height of micromirrors, represented by $d(i,j)$ where (i,j) indicates location of pixel, is modulated in a pixelated manner. Upon reflection of light by such spatially variable height and pixelated mirrors, phase of light is modulated $2kd(i,j)$, where k is a light propagation constant in free space, 2π/λ (Figure 1.4(b)). Typically, the range of $d(i,j)$ is chosen so that maximum displacement of micromirror $d(i,j)$ = d_{max} = λ/2, or 2π phase modulation, where lambda is wavelength of laser. The 2π phase

modulation maximizes diffraction efficiency in beam steering, by modulating phase 2π with stair-case approximated sawtooth blazed grating. For the fully modulated ($\Delta M = 2\pi$ in Eqn. (2)) discretized sawtooth blazed grating, the diffraction efficiency is given by:

$$\eta_1 = sinc^2(\frac{1}{m}) \tag{3}$$

, where m is the number of discrete stair level, η_1 is the diffraction efficiency of +1st diffraction order. Actual PLM has a non-linearity on the realizable phase level which is discussed in section 3.2. And simulation analysis of the effect of the non-linear phase level of PLM is described in section 3.3.3. The angle of diffraction is limited by PLM pixel pitch and wavelength of light, and given by λ/2p, where p is a period of PLM pixel. Currently the pixel period of TI-PLM is 10.8um. Therefore, the maximum diffraction angle is limited by several degrees.

1.2.1 PLM Beam Steering and Limitation

By PLMs, solid-state, fast, and efficient beam steering is feasible as far as the light is fully modulated in 2π. However, for lidar applications, longer wavelength of laser sources, for example, 905nm and 1550nm are commonly used. Employing longer wavelength with PLM imposes challenge in its phase modulation depth which is determined by the mechanical displacement range of the PLM pixel $d(i,j)$. For example, PLMs designed for visible wavelength at 633nm suffers from a low diffraction efficiency for 1550nm due to the insufficient phase modulation depth of 0.4π which is much less than 2π.

In Chapter 3, a method is described to optically enhance the phase modulation to overcome the challenge in insufficient phase modulation of PLM in general, including LCoS, LC, MEMS and others. By the method, insufficient phase modulation, or insufficient range of the mechanical displacement of micromirrors used with longer wavelength is optically enhanced by doubly

modulating phase with single PLM. Consequently, diffraction efficiency is increased at longer wavelength. For example, a PLM designed for wavelength of 633nm can be usable for wavelength of 905 and 1550nm while having a higher beam steering efficiency compared to beam steering by PLM without proposed optical enhancement.

1.3Novel Applications of MEMS-based Spatial Modulation Devices

MEMS-based spatial modulation devices have been actively research into variety of applications in recent years due to it light weighted, highly efficient, and incredible color reproduction properties. Other than lidar beam steering, it has also been actively researched for advance display system, holography, optical data storage, optical metrology, and biomedical instruments [9].

Holographic data is stored in a thick, light-sensitive optical material that uses optical interference patterns to store information, which is a highly attractive technology both in the scientific field and the industrial market due to its high-capacity data storage property. Different from the general magnetic and optical data storage technique, holographic data storage can record multiple images in the same area by using multiple reference beams with different angle during the recording process. Due to the excellent pixel switching speed, contrast ratios, and overall performance, DMD is worked as an ideal pixelated input device, used to provide the object information during the recording process. Below is an example of the recording process of holographic data storage.

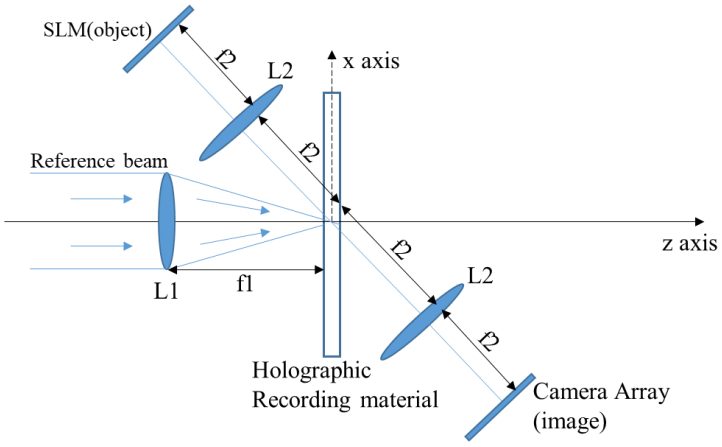

Figure 1.5 Schematic diagram of a Holographic data storage recording and readout process.

Holographic near-eye display is quite interesting the market and scientific field in the past few years. It reconstructs 3D images by utilizing interference between beams. Compare to other 3D display system, it has unique advantage which provide people superior immersion experience. Spatial Light Modulators in such display system used computer generated hologram pattern which provides high resolution dynamic display features.

Biomedical devices have undergone years of revolution and development in pursuit of higher resolution and better penetrating imaging results. Before, almost all optical biological imaging systems have been based on 2D imaging chip architecture. Modern microscopes provide 3D image reconstruction for biomedical imaging, such as photoacoustic microscope (PAM) and tomographic phase microscope (TPD). The latest developments in DMD are moving away from traditional optical projection displays into biomedical instruments. DMD devices with extremely high renewal rates may provide additional possibilities for biomedical imaging, such as real-time sensing and imaging.

1.4Summary and opportunities

In this chapter, two types of MEMS-based spatial modulation devices, DMD and PLM are introduced. DMD works as an amplitude spatial light modulator with a high refresh rate can be used as laser beam steering, which provide an efficient and course scanning into several diffraction orders determined by grating equation. The diffraction efficiency is governed by the phase profile of DMD that can be programmable by a synchronized short pulse illumination. The PLM modulates the phase of the incident beam. The MEMS-based PLM potentially has a high refresh rate comparable to DMD, which provide a fines scanning. The beam steering of the two devices, DMD and PLM can also be combined to form a 2D scanning for lidar application.

In this thesis, we first address stability of DMD based diffractive beam in diffraction efficiency and its sensitivity to environmental temperature. In chapter 3, we address PLM based beam steering focusing on enhancement of the diffraction efficiency by using Talbot self-imaging. Finally, we summarize potential pathway to implement those two techniques to laser beam steering modalities.

Chapter 2. Stability Evaluation of DMD Diffractive Beam Steering

2.1 Motivation

The diffractive DMD-based beam steering relies on a precise synchronization of the illumination pulse to micro mirrors' transitional state which is typically couple of microseconds [5,6]. Although this illumination mode is new, highly reliable and stable operation of DMD in the spatial light modulation mode was reported as well as is proven as various products over several decades [7,8]. We anticipate that the diffractive beam steering is also highly reliable. Though for the purpose of

stable beam steering operation utilizing the dynamic mirror transitional sate, a long terms stability as well as sensitivity of the synchronization timing with respect to variation of environmental temperature is of great interest.

In this Chapter, a long-term stability of DMD-based diffractive beam steering is reported under continuous operation of DMD based diffractive beam steering with 360Hz scan rate. A variation of mirror synchronization timing, consequently variation of diffraction efficiency under temperature variation of micro mirror array is also reported with ranges of 45 to 75 degrees C. Methods are also reported to keep the stability of DMD-based diffractive beam steering by adaptively controlling synchronization timing based on a look-up table under such temperature variation.

2.2 Stability Evaluation Methods

Figure 2.1 shows a schematic of experimental setup for long term stability testing of DMD based diffractive beam steering. A laser diode (LS9-220-8-S10-00, Laser Components) is collimated and illuminates the DMD with an 8ns pulse at an incident angle of 30 degrees. The 905nm wavelength incident beam is sequentially diffracted from -2nd to +2nd orders into five diffraction orders with LightCrafter 4500. An Aluminum surface mirror (98% reflectivity) is placed in the path of each diffraction orders to redirect diffracted beams into three avalanche photodiodes (C12702-04 Hamamatsu) connected to a single oscilloscope (DS1104Z plus, RIGOL). From a cover glass on the top of DMD micromirrors, the beam reflected and follows the same path of the 0th diffraction order. In total, time profile of six signals, 5 diffractions and 1 cover glass reflection were monitored by oscilloscope.

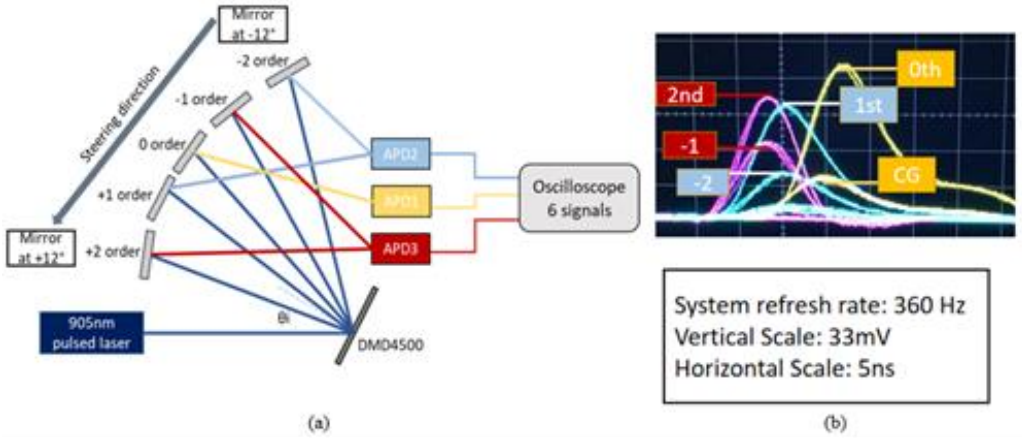

Figure 2.1 Schematic of stability evaluation experimental setup. Reprinted with permission from [15] © SPIE.

Figure 2.2 shows a picture of heat cycling testing setup. For the purpose of heat cycling test, two heating coils are placed around the DMD micro mirrors. Temperature of the surface of DMD mirror array is recorded by an infrared thermal imager (E40, FLIR).

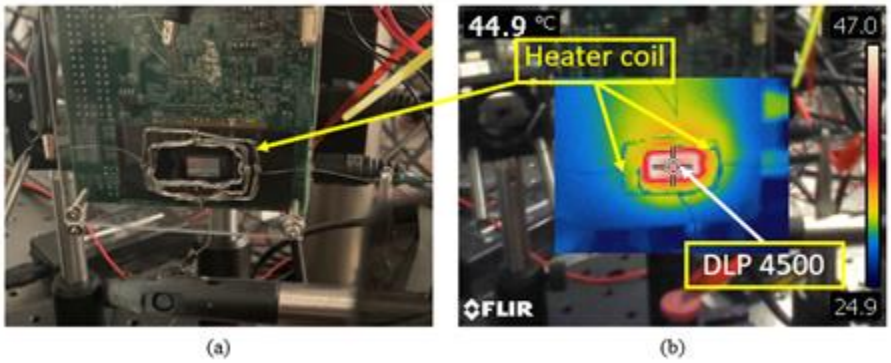

Figure 2.2 (a) Setup of heat cycling test. Heating coils are places placed at the vicinity of DMD; (b) Temperature image captured by thermal imager. Reprinted with permission from [15] © SPIE.

By applying a current to each coil, the temperature of the micromirror area of DMD is controlled as depicted in Figure 2.4 (a). The peak signal level of diffracted beam captured by APD, and DMD array temperature are plotted as a function of time in Figure 2.4 (a).

2.2.1 Long-term Stability Evaluation Experimental Result

Diffractive beam steering by DLP4500 was operated continuously for 350 hours under a room temperature (24 degrees C) without heatsink attached to the DMD chip. In Figure 2.3, the peak signal of five diffraction orders and cover glass are plotted with a linear trend line corresponding to each signal. The slope of each trend line is marked in red to evaluate the change in beam intensity. Since the signal of the beam reflected through the cover glass is not affected by time synchronization between DMD and laser pulse, the signal from the cover glass serves as a base-line data for comparison with other beam intensity signals. As can be seen from Figure 2.3, even though the light intensity signal fluctuates around the trend line, there is no significant downward trend from the beginning to end. The slope of all trend lines is less than the absolute value of 0.1. Therefore, we can say that the system has a high stability when working at room temperature for over 350 hrs.

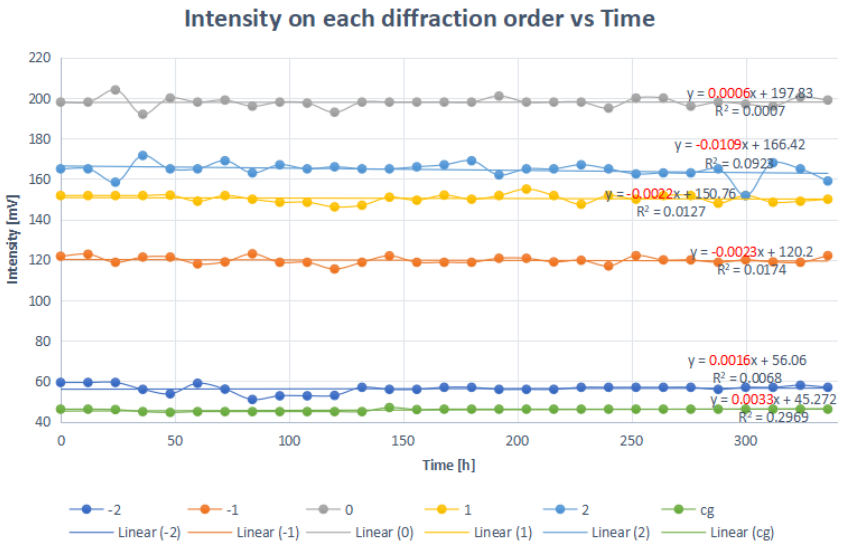

Figure 2.3 Results of continuously operating beam steering system under room temperature 25-degree C. Reprinted with permission from [15] © SPIE.

2.2.2 Heat Cycling Test Experimental Result

In room temperature at 25 degrees C, the temperature of DMD mirror array is about 45degree C. Figure 2.4 (a) shows the peak signal of each diffraction orders as a function of variation of temperature of DMD mirror array. When the micro mirrors' temperature exceeds 60 degrees C, the diffraction efficiency shows an obvious downward trend. And reached its lowest at 75 degrees C (the highest temperature given during the experiment). It was observed that the peak signal of the reflected light from the cover glass remained unchanged throughout the heat cycle. This proves that the experimental system was not, but only the change of the delay of the micro mirror was affected by the temperature. This was also confirmed by re-adjusting delay time while DMD mirror surface temperature was 75degree C.

To confirm that the decrease of the peak signal is due to the variation of delay, we changed the internal delay at high temperatures and monitored diffraction efficiency of each orders. Figure 2.4 (e) shows the signal profile under 75 degree C after increased by 125ns internal delay for each diffraction orders. The result indicates that even though signal goes down under high temperature, diffraction efficiency can be recovered by re-adjusting the delay, specifically by adjusting the internal time delay for each of the different diffraction orders. At 75 degrees C, we observed the peak signal levels of all the diffraction orders were recovered back to the level of diffraction efficiency for the array temperature of 45 degrees C.

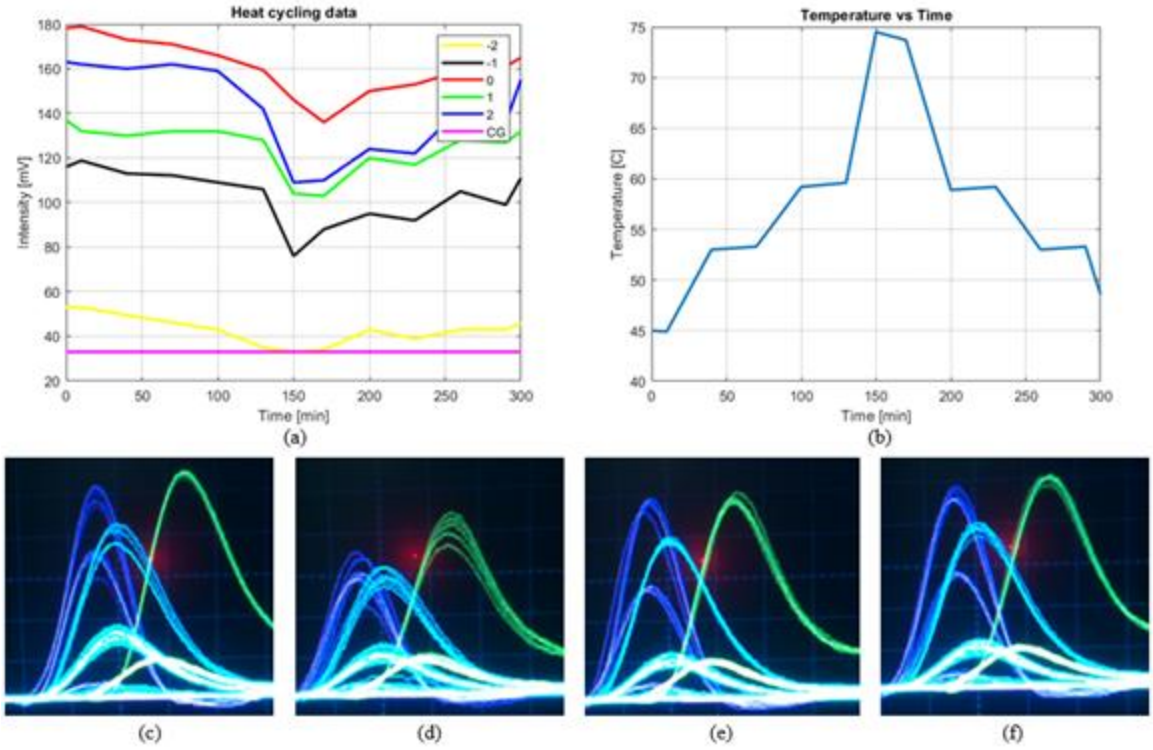

Figure 2.4 Representation of (a). Peak signal of each of diffraction order during heat cycling; (b). Temperature on the micromirror surface during heat cycling; signal profile profiles; (c) at 0min; (d) at 150min under highest temperature on DMD micromirror surface (75 degree C); (e) at 150min under highest temperature 75 degree C after increased the internal delay on each diffraction order by 125ns; (f) at 300min back to room temperature 25 degree C with 48 degree C on the micromirror surface of DMD. Reprinted with permission from [15] © SPIE.

Table 2.1 tabulates peak signal of each diffraction order concerning different internal delay increments. At 75 degrees C, the results tell by increasing delay time, 125ns results in the highest light-strength increment for 1st and 2nd orders, increasing delay time results in the highest light-strength increment for 0th, -1st and -2nd orders. In our experiment, time precision is limited to 62.5 nanoseconds by clock cycle of the micro controller, Arduino Uno. The time resolution might not meet the optimum delay especially for -1st order. We also adjusted internal delay time at 60

degree C and 53degree C. At 66 and 53 degrees C, the additional internal delay is less than that of the maximum temperature 75 degrees C.

Table 2.1 Signal change on each diffraction order after adjusting different amount of internal delay times (in nanoseconds) under 75 degree C highest temperature. Reprinted with permission from [15] © SPIE.

Temperature [℃]	**Delay adjusted [ns]**	**2nd order [mV]**	**1st order [mV]**	**0th order [mV]**	**-1st order [mV]**	**-2nd order [mV]**
75	+62.5	+35	+25	+20	+10	+3
	+125	+47	+30	+15	-5	_
	+187.5	+11	_	-3	-6	-2

2.3 Discussion: Possible way to increase the Stability of DMD Beam Steering

There are several ways to maintain the stability of DMD diffractive beam steering method under temperature variation, besides actively cooling the DMD chip with heat sinks. According to the experimental data, we can optimize the internal delay time of each diffraction order as a function of temperature for example by using a lookup table to achieve a stable time synchronization at different temperatures. In the experiment, resolution of timing adjustment was limited by clock cycle of micro controller, 62.5ns. Even higher time resolution is feasible with a programmable timing element (for example DS1023, Dallas Semiconductor) between the Arduino and laser source which adds delay with 0.25ns timing precision. This allows the Arduino microcontroller to adjust delay with much higher time precision.

2.4 Summary

In this chapter, we evaluated stability of digital micromirror device based diffractive beam steering. We observed the high stability property of diffractive a beam steering after 350 hrs. of continuous

operation. As of May 6th, 2021, accumulated operation time is 3600 hours in total as the experimental system is still operating while keeping diffraction efficiency as the same level to the initial diffraction efficiency. At the same time, we evaluated the effect of increased temperature of mirror array, especially on timing in synchronization between the laser pulse and micromirror transition time and quantified this effect by adjusting the internal delay. The results confirmed a stable and long-term operation of DMD beam steering feasible by adjusting synchronization timing of ns- laser pulse to mirror transition in an adoptive manner for example by using a look-up table. Figures and contents in this chapter are reprinted from reference [15] with permission by SPIE.

Chapter 3. Diffraction Efficiency Enhancement of PLM Infrared Beam Steering

3.1 Motivation

As described in chapter 1, for the purpose of infrared beam steering applications, PLM designed at visible wavelength suffers from low diffraction efficiency at a longer wavelength due to its insufficient phase modulation depth. For example, using PLM designed at wavelength of 633nm used at a different wavelength λ, the maximum 2π phase modulation depth will change by a factor of $633/\lambda$. When the wavelength is longer as compare to the designed wavelength, the phase depth will decrease as well as the diffraction efficiency.

In this chapter, a method for doubling the phase modulation depth is proposed, using the Talbot effect, we do a pixel matching to cascading the image of the PLM (from Texas Instruments) on top of itself so that phase depth can be increased. The doubled phase depth method we call it dual

phase modulation, detailed method, phase analysis, comparison between dual modulation and single modulation, and diffraction efficiency enhancement results will be discussed in the following sections.

3.2 Diffraction Property of PLM

To discuss PLM beam steering, the diffraction property behind it needs to be introduced. As mentioned in chapter 1, Texas Instruments PLM consists of a pixelated micromirrors that change height of the mirror along the direction of its the surface normal. By upload the computer-generated hologram pattern through the HDMI port, we can display different period grating with different phase modulation depth on the PLM.

As depicted in figure 3.1, PLM works as a digital reflection hologram steering the beam in two dimensions, the normal incident plane wave works as the reference beam with a propagation vector direction pointing to the positive direction of z-axis. We first determine the desired object field which is the steered beam and compute the interference pattern of the steered beam with the reference beam, then encoding the CGH into the PLM readable form [10].

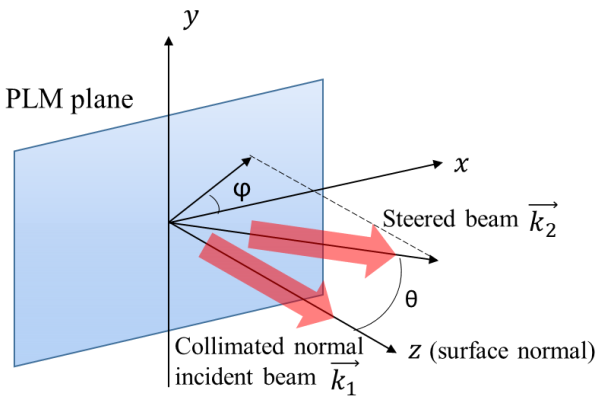

Figure 3.1 Schematic of PLM beam steering.

The magnitudes of the propagation vectors are the same, since they use the the same wavelength and interference in the same media. Thus, the magnitude of both propagation vectors is:

$$k = \left|\overrightarrow{k_1}\right| = \left|\overrightarrow{k_2}\right| = \frac{2\pi n}{\lambda} \tag{4}$$

The directions of the propagation vectors are defined by the angles θ and φ relative to the positive direction of x y z-axis. The resulting propagation vectors are:

$$\overrightarrow{k_1} = k\hat{z}$$

$$\overrightarrow{k_2} = k(\sin\theta\cos\varphi\,\hat{x} + \sin\theta\sin\varphi\,\hat{y} + \cos\theta\,\hat{z}) \tag{5}$$

The grating vector indicates the direction and space of the grating plane that results from the interference fringe pattern. The magnitude of the grating vector can be represented as:

$$K = \left|\vec{K}\right| = \frac{2\pi}{\Lambda} \tag{6}$$

where Λ is the fringe space resulting from the interference of the incident beam and steered beam.

The grating vector can also be found by combing the propagation vectors. From the Bragg Condition, we can have:

$$\vec{K} = \overrightarrow{k_1} - \overrightarrow{k_2} \tag{7}$$

With different period CGH displayed on the PLM, the steered beam will result in different amount of diffraction angle. In our experiment, we use un-slanted grating that is incident beam and steered beam are all in x-z plane. 2 pixels per grating period CGH pattern or binary grating results in the maximum diffraction angle, which has the equal diffraction efficiency on the $+1^{st}$ and -1^{st} order, 40.1% in theory. The 4 level and 10 level sawtooth grating pattern, or blazed grating are also used in the experiment. Fig. 3.2 depicts the configuration of PLM 2 pixels period binary grating and 4 levels sawtooth blazed grating. Horizontal axis in Fig 3.2 is the grating period, while vertical axis is the optical displacement or phase depth before reflection. In theory, π phase depth results in high

diffraction efficiency for binary grating while 2π phase depth results in high diffraction efficiency for blazed grating.

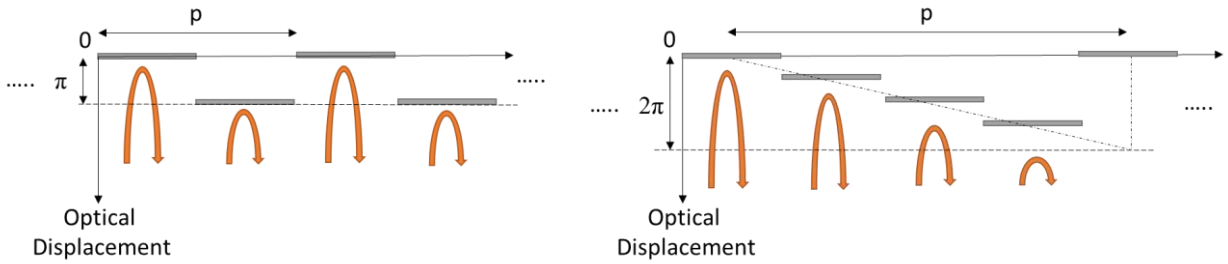

Figure 3.2 PLM binary (left) and blazed (right) grating configurations.

The PLM array is 960x540 elements, and 4 memory cells are under each element making the addressable memory 1920x1080. The pixel height of PLM has 16 different levels that can be adjusted by giving different combinations of 1 or 0 logic to each memory cell. Figure 3.3 depicts 16 types of combination of logic that results in 16 levels of pixel height of PLM. When creating the grating CGH for PLM, we first determine the aimed phase depth, grating period and orientation, then encoding the 960x540 CGH to 1920x1080 PLM readable form by using the information from Fig 3.3. As we can see in Fig 3.3, the theoretical displacement of 16 levels of pixel height is non-linearly arranged. Compare to linearly phase level distribution, non-linearity will cause decreasing in diffraction efficiency which will be discussed in the simulation section.

		15		14		13		12		11		10		9		8			
Location	Voffset-Vbias	MSB [nm]		MSB-1[nm]		MSB-2[nm]		MSB-3[nm]		MSB-4[nm]		MSB-5[nm]		MSB-6[nm]		MSB-7[nm]			
Theoretical		100%		87.66%		72.24%		65.58%		55.19%		46.44%		40.86%		37.14%			
Pixel Addressing	row \ col	col	col+1	col	col+1	col	col+1	col	col+1	col	col+1	col	col+1	col	col+1	col	col+1		
	row	1	1	1	1	1	1	1	1	0	1	0	1	0	1	0	1	E3	E4
	row+1	0	0	1	0	0	1	1	1	0	0	1	0	0	1	1	1	E1	E2

7		6		5		4		3		2		1		0			
MSB-8[nm]		MSB-9[nm]		MSB-10[nm]		MSB-13[nm]		MSB-11[nm]		MSB-12[nm]		MSB-14[nm]		LSB[nm]			
18.37%		12.01%		6.57%		5.37%		4.06%		2.16%		0.83%		0.00%			
col	col+1	col	col+1	col	col+1	col	col+1	col	col+1	col	col+1	col	col+1	col	col+1		
1	0	1	0	1	0	0	0	1	0	0	0	0	0	0	0	E3	E4
0	0	1	0	0	1	1	0	1	1	0	0	0	1	1	1	E1	E2

Figure 3.3 PLM 4bit 16 non-linear phase mapping.

3.3 Optical Enhancement of Phase Modulation

Figure 3.4 schematically shows the architecture to enhance phase modulation depth, consequently diffraction efficiency for laser beam steering. A collimated and linearly polarized Laser beam/pulse goes through a 4f, 1:1 relay where a tilted mirror with a center hole is placed at the back focal point of the first lens. A vertically polarized (VP) and collimated light is deflected by a polarized beam splitter (PBS), followed by passing through a Quarter Wave Plate (QWP) that converts linear polarization (LP) to right circular polarization (RCP). Upon interaction of the RCP light with PLM, spatial phase is modulated by $2kd(i,j)$. PLM reflects and modulates phase of light while changing the polarization from RCP to left hand circular polarization (LCP). The 2nd interaction with QWP changes polarization of light from LCP to horizontally polarized (HP) light. The mirror M1 is placed at a half of the Talbot distance from the PLM as described later. The reflected light by M1 is a HP light, therefore it goes through the PBS and is converted to RCP by the 3rd interaction with QWP. Finally, the light is modulated by the PLM with the same phase modulation profile and reflected to the direction along the incident laser beam via QWP and PBS. After the laser beam is doubly modulated, the laser beam diffracted towards direction defined by the CGH pattern displayed on PLM. The diffracted beam is reflected by the mirror placed in the 4f 1:1 collimating optics followed by a collimating optics for beam steering.

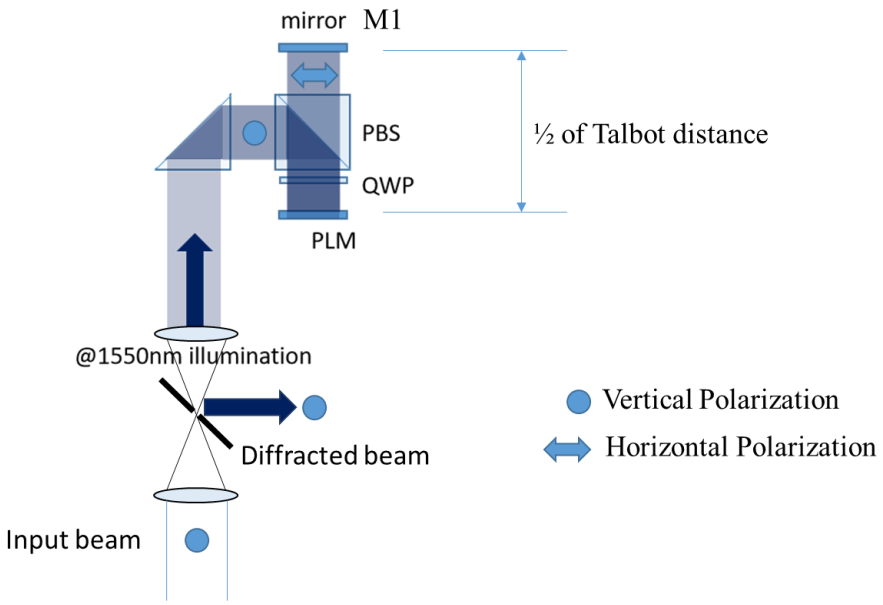

Figure 3.4 Schematic of optical enhancement of phase modulation experiment with polarization indicated.

The key design parameter of the system is to doubly modulate phase by using single PLM of a period of CGH, wavelength λ and optical path length between PLM and mirror M1. The spacing between PLM and M1 is half of the Talbot distance which is given by:

$$z_{Talbot} = \frac{2p^2}{\lambda} \tag{8}$$

where p is periodicity of phase modulation pattern of PLM. At the Talbot distance, a periodic phase pattern is reproduced without employing imaging optics. The effect is known as Talbot self-imaging. The Talbot self-imaging is commonly referred in reproducing its periodic amplitude profile. The PLM which is placed at the Talbot distance of modulation pattern of PLM doubly modulates the phase. This double modulation optically increases mechanical traveling range of micromirror by factor of 2. Upon reflection by PLM, the RCP changes polarization. The QWP finally change polarization state from LCP to VP. Interaction of VP light with PBS deflects light towards direction of incident light. The diffracted beam will be at an angle to the incident beam,

so that the diffracted beam will be reflected off by the mirror with the hole in the center and separating it out from the path of the incident beam.

3.3.1 Talbot Imaging in PLM Dual Modulation

In the previous section, we briefly talked about the Talbot Effect that is a diffraction phenomenon occurs for periodic objects illuminated with laser light. If the object periodicity or say grating period is larger than the illumination wavelength, the maximum extent of the object's angular spectrum is limited to small angles. The angular spectrum of a laser beam transmitted through a weak phase grating consists of three plane waves, which combine to form periodic replications of the original phase distribution along the z axis as depicted in figure 3.5 [11].

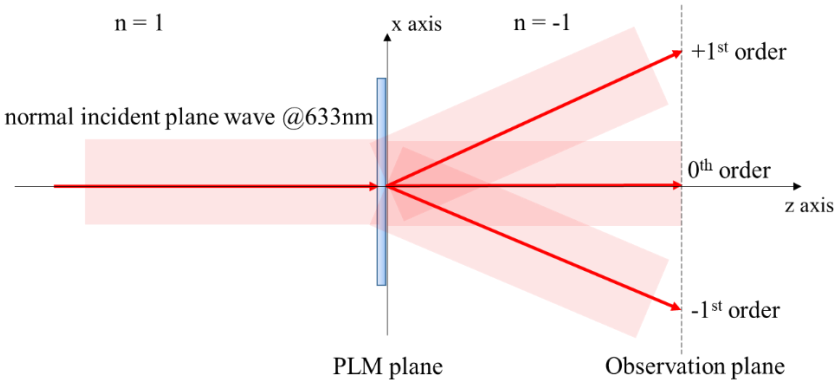

Figure 3.5 Talbot imaging illustrated as three-beam diffraction.

In the observation field, the observation plane is sequentially location with interval length z_{base}. The PLM phase grating and its pure phase reconstruction are labeled as A planes. B planes are locations where the phase modulation becomes amplitude modulation. C planes are the conjugate phase reconstructions, and D planes are the reversed contrast amplitude reconstructions as illustrated in Figure 3.6. Notice that the plane with the same phase information as the PLM plane is location at one Talbot distance.

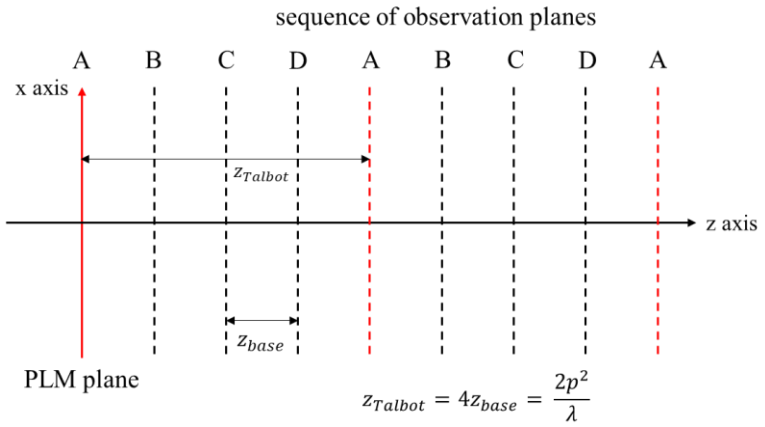

Figure 3.6 Spacing periodicity of the sequence observation planes.

Therefore, for different period grating with different illumination wavelength, we will get the repetition of phase distribution at different distance with respect to PLM plane. Table 3.1 illustrates the required Talbot distance for 2 pixels and 4 pixels per period gratings at 633nm, 905nm, and 1550nm wavelength.

Table 3.1 Required Talbot distance for 2 pixels and 4 pixels per period gratings at 633nm, 905nm, and 1550nm wavelength.

Light Source		633nm	905nm	1550nm
Z_{talbot}	d = 2p = 21.6um	1.4741mm	1.0310mm	0.6020mm
	d = 4p = 43.2um	5.8965mm	4.1243mm	2.4081mm

To apply PLM for beam steering purpose, the grating period we need to use to obtain a continuous beam steering better range from 2 to 20 pixels. For 20 pixels per period grating, one order of Talbot distance goes up to 103.11mm. The required Talbot orders for different pixel per period grating with 905nm illumination are listed in Table 3.2.

Table 3.2 Required Talbot orders and Talbot distance for 2 to 20 pixels per period grating with 905nm illumination.

Non-integer pixel period	Talbot order m	Z_t [mm] at 905nm
20.000	1	103.1071823
10.000	4	103.1071823
6.667	9	103.1071823
5.000	16	103.1071823
4.000	25	103.1071823
3.333	36	103.1071823
2.857	49	103.1071823
2.500	64	103.1071823
2.222	81	103.1071823
2.000	100	103.1071823

For 20 pixels per period grating, the Talbot distance is relatively large compared to the small pixel period grating. Therefore, talbot image at large distance needs to be confirmed. To visualize the Talbot phase image of single modulated PLM, a Linnik Interferometer is used as depicted in figure 3.7. A 633nm He-Ne laser is used in this setup. With the reference mirror and lens array, the phase image of the PLM can be visualized by the camera.

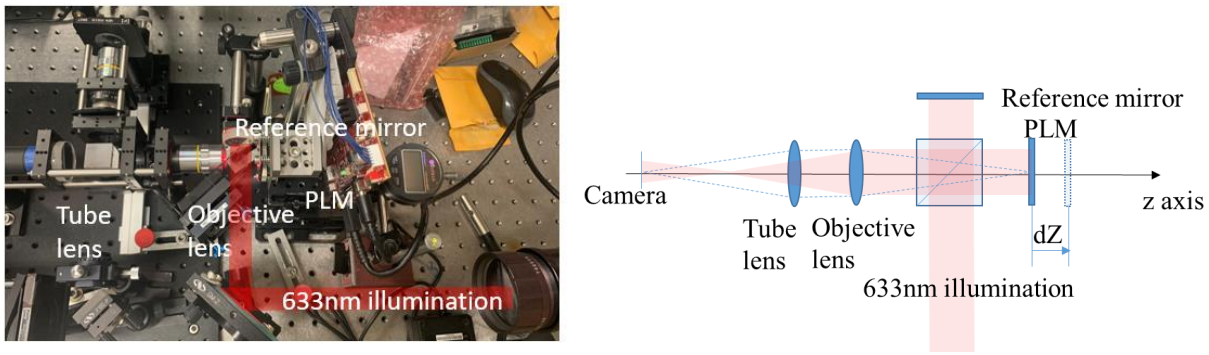

Figure 3.7 Experiment setup of the Linnik Interferometer (left); Schematic layout corresponding to the experiment setup (right).

By switching between coherent and incoherent light source, we can visualize both the incoherent intensity image and phase image of PLM. During the experiment, incoherent white light source is first be used to confirm the PLM is at the in-focus location of the objective lens. Then, change back to coherent 633nm light source, slightly move the PLM along z axis observe the phase image and record the distance dz.

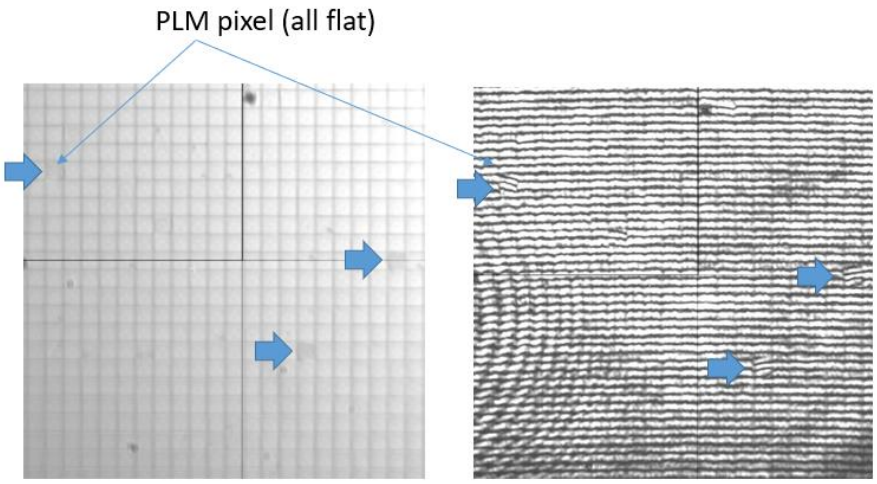

Figure 3.8 Amplitude (left) and phase (right) image of all flat PLM at the in-focus location.

The amplitude and phase image of PLM at the in-focus location are depicted in figure 3.8. There are several dark pixels in the amplitude image corresponding to the discontinuous fringe in the

phase image. The tilt of the fringe represents the tilt pixel of PLM pixel array. The dark pixel observed in the incoherent image is explained as follows. The tilted PLM pixel reflects light from the pixel outside to the pupil of the Linnik microscope interferometer, consequently the bright ness of the pixel decreases. These tilt pixels as while as the gap between pixels (refer as fill factor of PLM is less than 1) and nonlinear phase depth property of PLM also cause the decrease in diffraction efficiency.

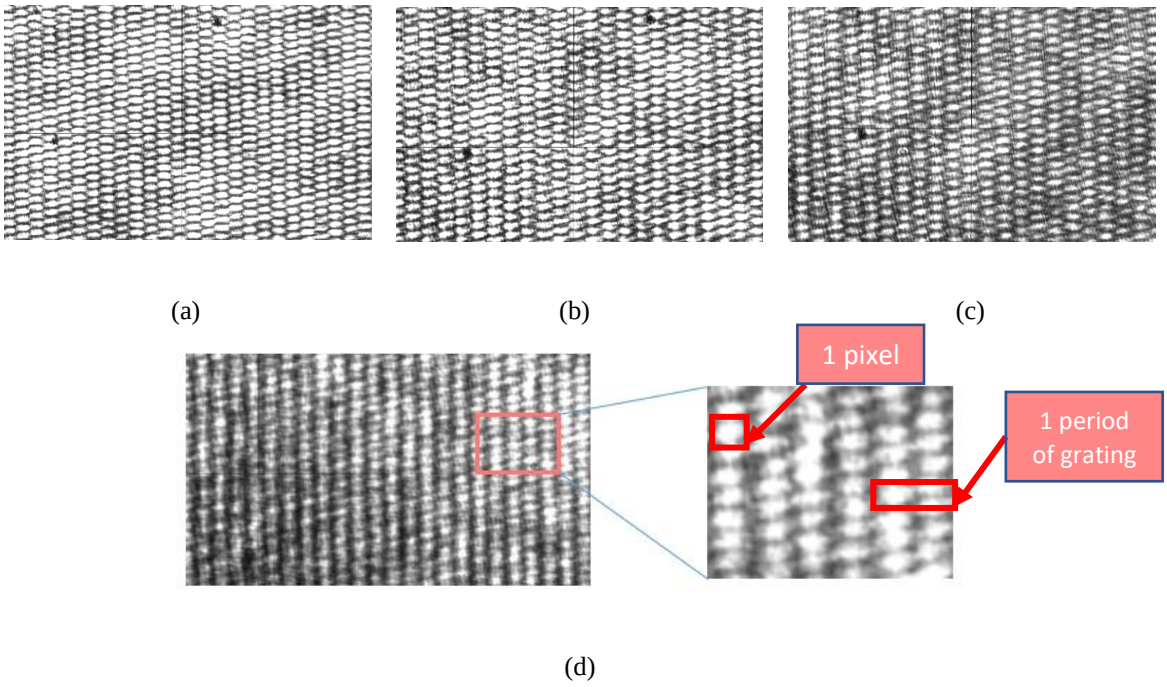

Figure 3.9 Phase images of a 2 pixels per period binary grating of PLM at different integer times of Talbot distance or Talbot order. (a) is at dz = 22mm almost equivalent to 15 Talbot order for 633nm illumination, (b) is at dz = 73.6mm or say 50 Talbot order, (c) is at dz = 110.55mm corresponding to 75 Talbot order, and (d) is at dz = 147.1mm equal to 100 Talbot order for 633nm wavelength.

Phase images in figure 3.9 are the results of a 2 pixels per period binary grating. The adjacent fringes have a half fringe period offset indicates a π modulated phase depth of PLM. At 100 Talbot order, which is equivalent to 1 Talbot order for a 20 pixels per period phase grating, the phase

distribution as zoomed in in figure 3.9 (d), is still recognizable and same as the in-focus phase image. This confirmed at large Talbot distance, the phase repetition or say Talbot imaging of the PLM grating is still feasible.

To confirm dual modulation works with the Talbot imaging, the setup is modified into Twyman Green Interferometer to visualize the Talbot image of dual phase modulation. As depicted in figure 3.10, a half mirror is used as the reference arm to interfere with the beam from PLM. Using half reflection mirror instead of full reflection mirror is to balance the intensity ratio between the reference beam and the diffracted beam that maximizes fringe contrast.

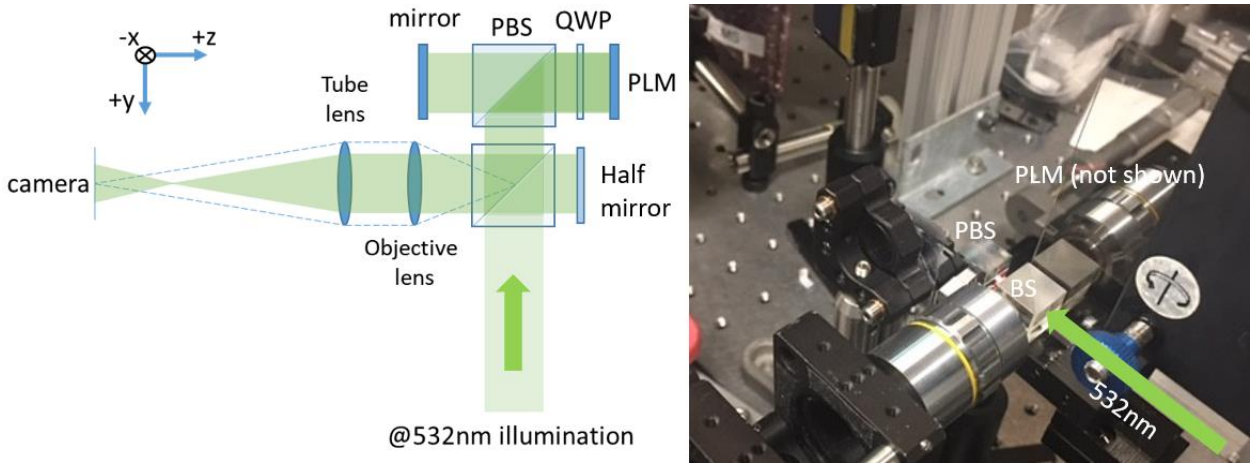

Figure 3.10 Experimental setup of the Twyman Green Interferometer (right); Schematic layout corresponding to the experiment setup (left).

The distance between PLM and mirror is set to the half Talbot distance so that the image of the PLM has the same phase distribution of itself. This is called Talbot self-imaging. In this experiment, 532nm wavelength light source is used. As illustrated in table 3.3, if the phase of the output beam is doubled, a $\pi/4$ modulated phase depth of a 2 pixels per period grating pattern will turns to be a $\pi/2$ modulated phase pattern. In visualization by Twyman Green phase visualization setup we expect that a $\pi/2$ modulated phase depth of a 2 pixels per period grating pattern will turns to π

modulated phase pattern, which will result in the same fringe pattern as depicted in figure 3.9. For the case with π modulated phase depth of a 2 pixels per period grating pattern will turns to 2π modulated phase pattern in dual modulation. Consequently, it shows a continuous fringe pattern as all flat fringe pattern in figure 3.8. The single and dual phase modulation can be switched by rotating the QWP placed between the PBS and PLM.

Table 3.3 Phase mapping and phase depth illustration between single and dual modulation at 633nm and 532nm wavelengths. (Phase level information refers to section3.2)

PLM level		6	7	9
Single modulation theoretical displacement	@633nm	12.02%	18.37%	40.86%
	@532nm	14.29%	21.86%	48.62%
Dual modulation theoretical displacement	@532nm	28.58%	43.72%	97.23%
Dual modulation Phase depth	@532nm	~ π/2	~ π	~ 2π

Figure 3.11 shows the phase images of dual modulation at Talbot distance. The discontinuity of the fringe pattern is as expected. As labeled in the red and blue dash line, the level 6 grating pattern in single modulation modulates π/4 depth while in dual modulation this depth is doubled to be π/2 phase depth. Therefore, in the interferometer, we expect to see half fringe space offset. Same for level 7 who has a π/2 phase depth in single modulation and π phase depth in dual modulation results in half fringe space offset, and level 9 has a 2π phase depth in dual modulation expect to see a continuous fringe pattern from the Twyman Interferometer. This confirmed the feasibility of the Talbot image based dual phase modulation.

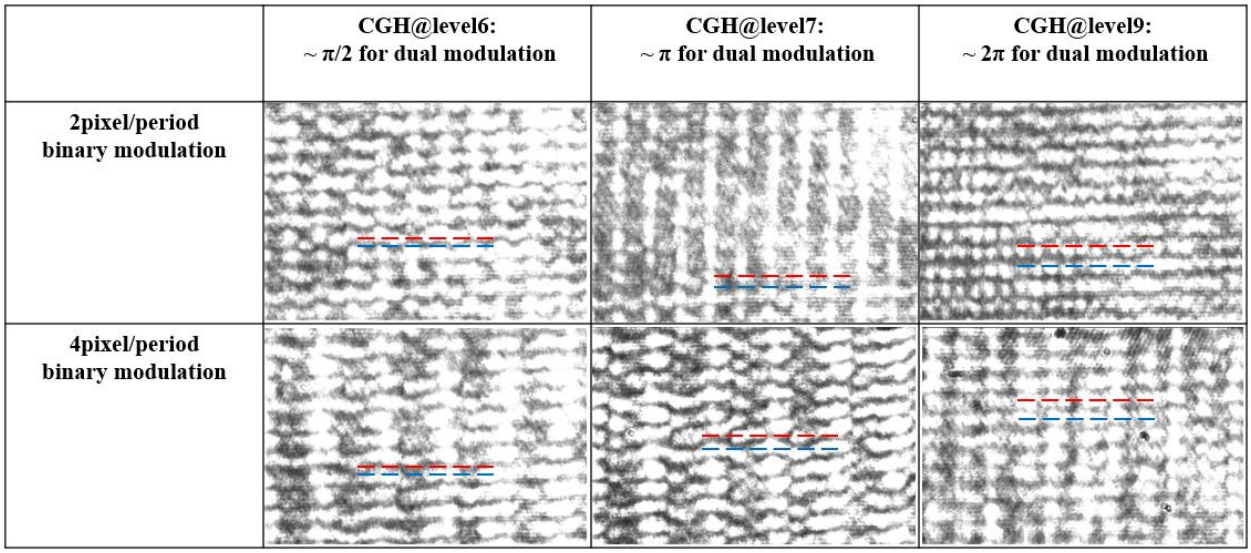

Figure 3.11 Dual modulation phase image of different depth and different period phase grating.

3.3.2 Phase Depth Analysis of Single and Dual Modulation

Phase Light Modulator (PLM) modulates phase of laser in 2-dimensional and a pixelated manner. The laser illuminates PLM and is modulated by a 960x540 array of reflective pixel elements having a pixel period of p=10.8 um. The phase is modulated in a way such that each of the pixel shifts along the direction normal to the array plane currently with 16 discrete levels (Fig. 3.12). The 1st order diffraction angle is determined by λ/d where λ is a wavelength, and d is a periodicity of CGH pattern. The maximum diffraction angle is given by $\lambda/2p$.

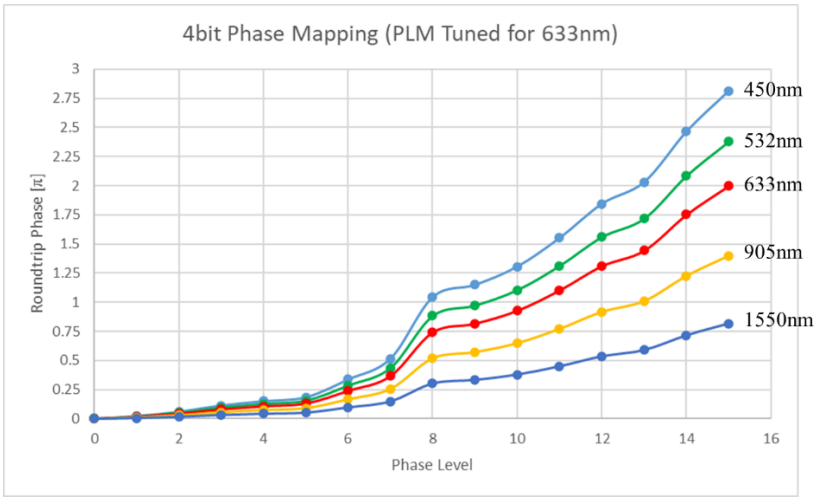

Figure 3.12 Roundtrip 4-bit phase mapping at different wavelength of single modulated PLM tuned for 633nm.

For an efficient and single point beam steering, a saw tooth shaped phase profile with a modulation depth of 2π is commonly used. The phase profile is known as a blazed grating. Since PLM is a digitally controlled device, the spatial phase profile in implemented in a discretized manner. The continuous and saw tooth "blazed" phase profile is approximated by a discontinuous stair-case phase profile. The diffraction efficiency of such an ideal stair-case profile is analytically formulated in next section. However actual phase levels of PLM are nonlinearly spaced as depicted Fig. 3.12. Also, as wavelength becomes longer, the maximum phase depth decreases. The level 15 phase depth is less than 1.5π for 905nm and less than π for 1550nm. The insufficient linearity and phase depth all cause decreasing in the diffraction efficiency. In next section, the simulations of the diffraction efficiency using Rsoft will be shown.

If we successfully aligned the dual modulation system and the phase image is perfectly at integer number of Talbot distance, the phase depth will be doubled which gives us more degree of freedom for infrared applications of PLM. As depicted in Fig. 3.13, the maximum phase depth is large than 2.5π for 905nm illumination and large than 1.5π for 1550nm illumination.

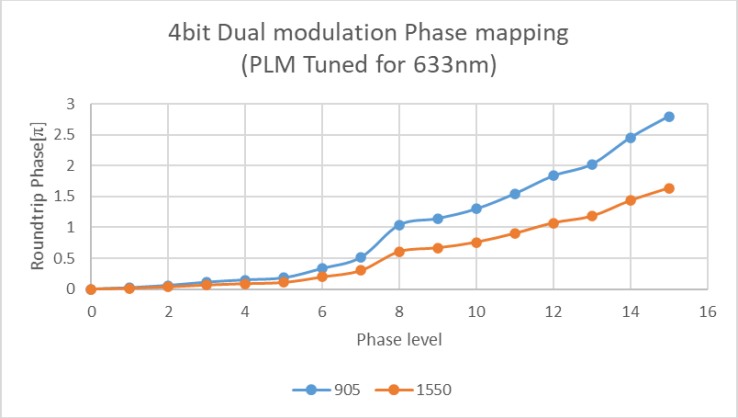

Figure 3.13 Roundtrip 4-bit phase mapping at infrared wavelength of dual modulated PLM tuned for 633nm.

3.3.3 Diffraction Efficiency Simulations

As introduced in chapter 1, PLM consists of pixelated micromirrors that change height of the mirror along the direction of surface normal. Fig. 3.14 shows a simulation configuration of a 3-by-3 array of pixels arrangement by using Rsoft. At 2D diffraction mode, the phase level, pixel gap, and pixel tilt of individual pixel can be simulated, and tell us how much diffraction efficiency will be for different types of grating. A group of pixels is created, and it expands infinitely in the x-y plane.

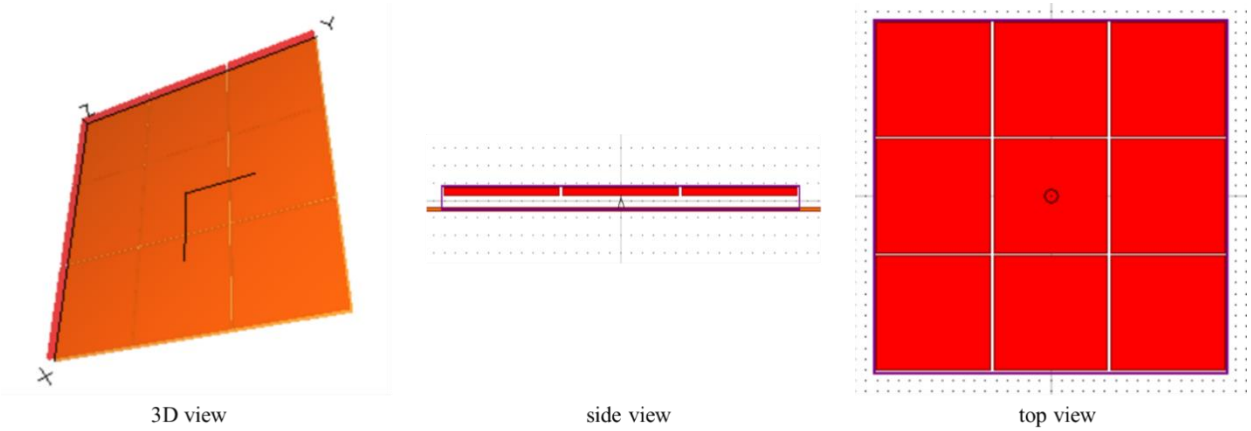

Figure 3.14 Configurations of PLM beam steering simulation.

When 0 phase level is given to each pixel in Fig. 3.14, we have all flat pixel array. Ideally, we will have 100% of efficiency from the reflection of an all-flat PLM. In fact, there are gaps between pixels with actual 1-dimensional fill factor (pixel width/pixel period) equals to 0.972 and estimated random tilt (between 0 to 0.3degree) of pixels. The periodic gap between pixels will form a grating shape which diffract the beam into higher orders and cause decrease in efficiency on 0^{th} order, and random tilt break the periodicity which also decrease the efficiency due to the wavefront error induced by the random tilt. Fig 3.15 shows the diffraction efficiency simulation when 0 phase level is allocated to each pixel. To analyze how fill factor and random tilt affect the output beam intensity, two simulations are conducted as depicted in Fig.3.15 at 633nm. One is ideal all-flat PLM that has an almost 90% output when launch angle (incident angle) equals zero. The other one is all-flat PLM with actual fill factor less than one and random tilt of each pixel. As we can see from Fig. 3.15, at 0degree incident, the diffraction efficiency of 0^{th} order decreased compare to the ideal case. And the output efficiency on the 0^{th} order only have almost 65% diffraction efficiency, which agrees with the experiment result that will be mentioned in section 3.4.

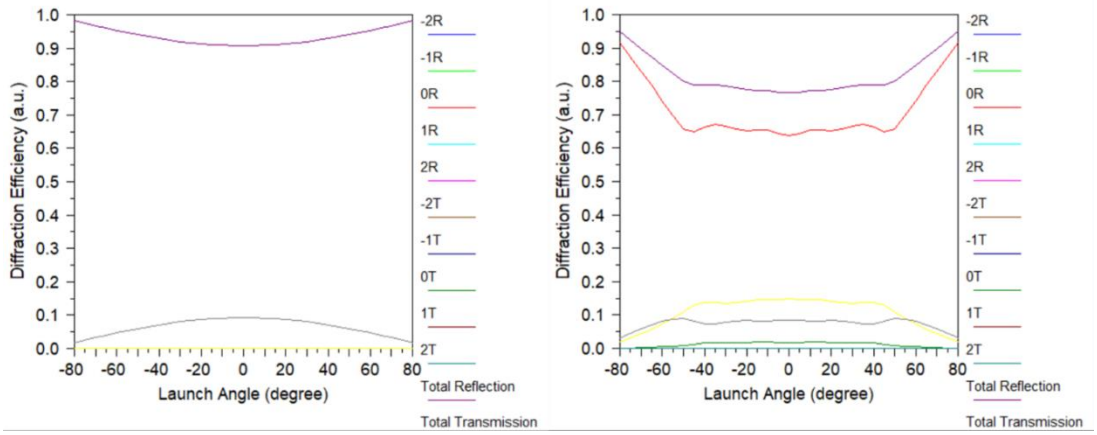

(a) (b)

Figure 3.15 Simulation of all "flat" pixel array. (a) 0^{th} order refection ideal case, no gap between pixels (fill factor = 1), and no random tilt of pixels; (b) 0^{th} order diffraction efficiency with fill factor = 0.972 and random tilt (between 0 to 0.3degree) of pixels.

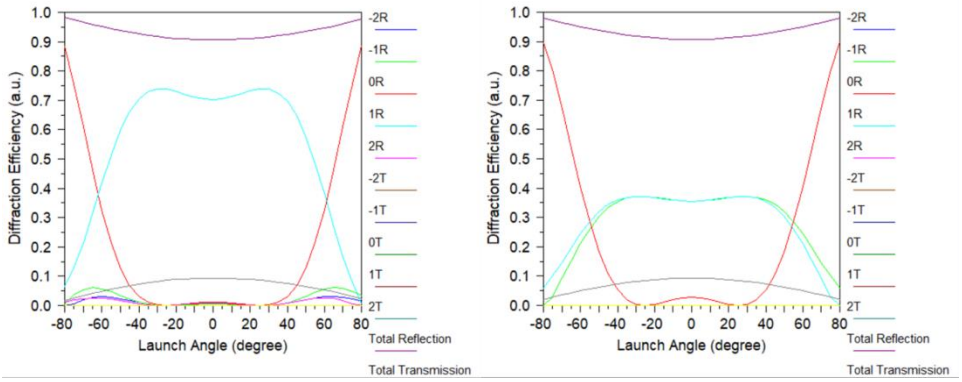

Figure 3.16 Ideal diffraction efficiency simulation of discretized sawtooth grating (left) and binary grating (right). In the simulation, the phase levels are linearly distributed with fill factor equals to one and no random tilt of pixels.

Fig 3.16 and Fig. 3.17 show the diffraction efficiency simulation of ideal and real case for both blazed and binary gratings. The decrease in fill factor and increase of randomness of pixel tilt cause almost 10% loss for binary grating and almost 20% loss for the blazed grating. These two figures are all single modulation simulation. The decreased diffraction efficiency will even be smaller for infrared applications because for the same mechanical tilt of the mirror, RMS wavefront error induced by the random tilt of the pixel inversely scales with the wavelength.

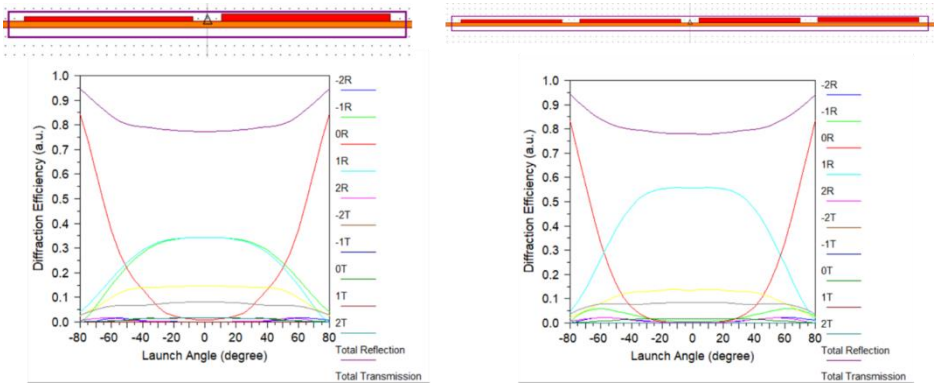

Figure 3.17 Diffraction efficiency simulation of discretized sawtooth grating (right) and binary grating (left). In this simulation, the phase levels are non-linearly distributed with fill factor = 0.972 and random tilt (between 0 to 0.3degree) of pixels.

Fig. 3.18 shows the diffraction efficiency simulations of single and dual modulation for 4-level blazed grating with 2π phase depth at 633nm and 0degree of incident angle. Instead of being launch angle, the horizontal axis is now wavelength range from 500nm to 2000nm. For single modulation, we have the peak of the diffraction efficiency curve occurs at around 0.6μm, and diffraction efficiency goes less than 40% when the wavelength is higher than 0.9μm. While for dual modulation, the peak is shifted to around 1.25μm and the diffraction efficiency is higher than 40% between 0.9μm to 1.9μm. This also confirmed our benefit of dual modulation system.

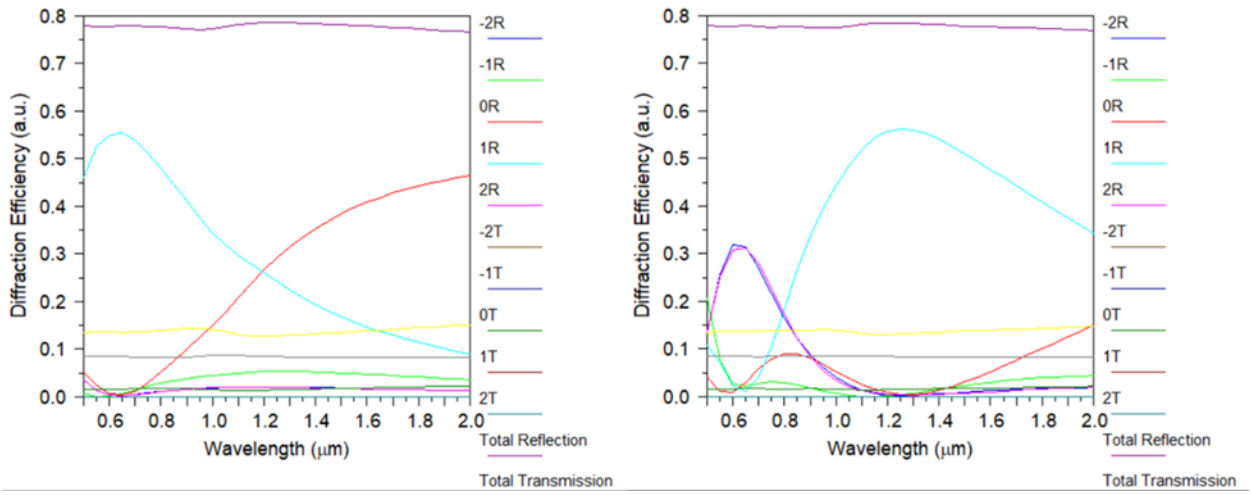

Figure 3.18 Diffraction efficiency vs wavelength simulation of non-linear discretized sawtooth grating, with fill factor = 0.972 (in 1D) and random tilt (between 0 to 0.3degree) of pixels. Left diagram is single modulation, right diagram is dual modulation.

To visualize the effect of non-linearity and pixel random tilt with respect to wavelength increasement. Simulations results are listed in Table 3.4 and Table 3.5. As we can see from the

table, both for single and dual modulation, non-linearity and random pixel tilt all cause almost 10% loss in diffraction efficiency for blazed grating. But no significant loss for binary grating (less than 5%).

Table 3.4 Discretized 4-level sawtooth blaze grating diffraction efficiency simulation with 1D fill factor equals to 0.972.

	Single Modulation	**Dual Modulation**
No tilt pixels, Linear phase level	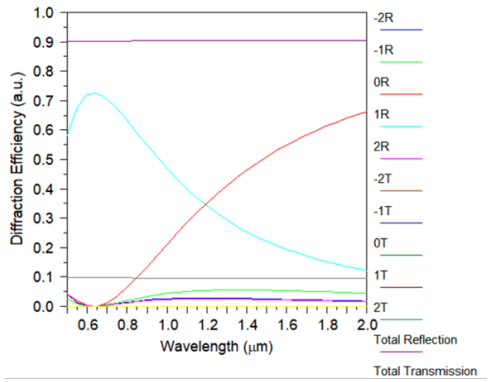	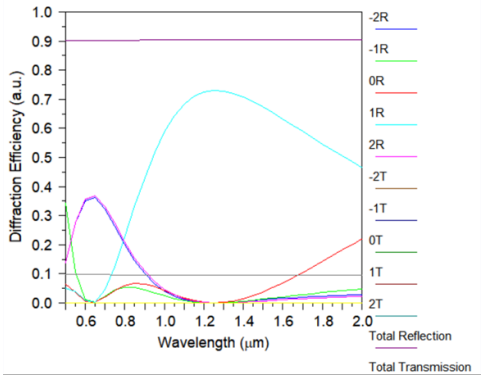
No tilt pixels, Non-linear phase level	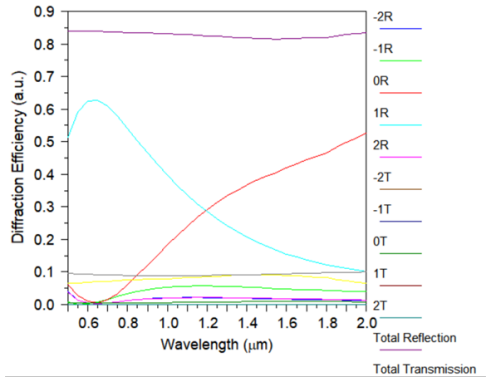	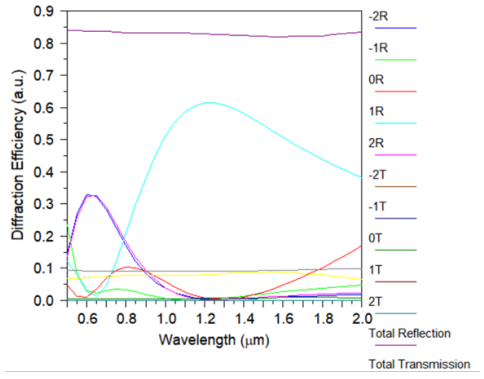

With tilt pixels, Non-linear phase level	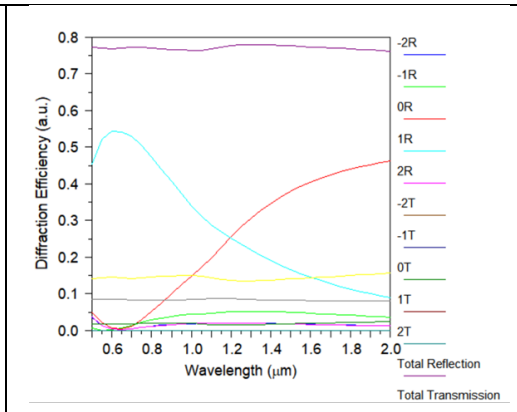	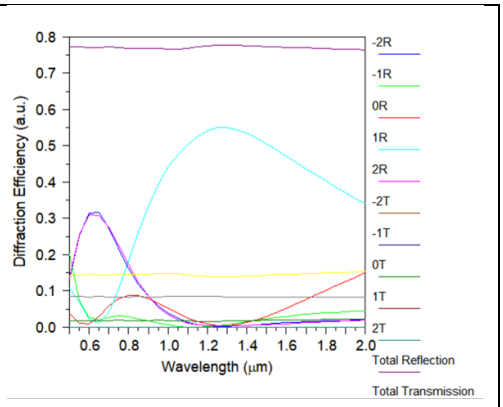

Table 3.5 Binary grating diffraction efficiency simulation with 1D fill factor equals to 0.972.

	Single Modulation	**Dual Modulation**
No tilt pixels, Linear phase level	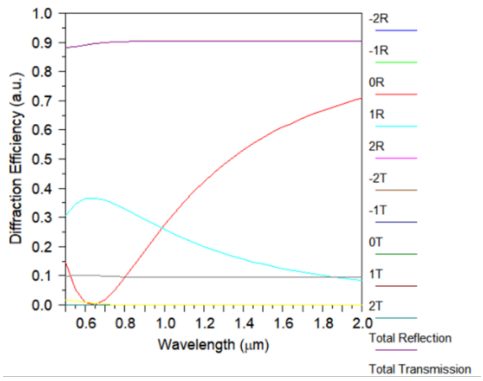	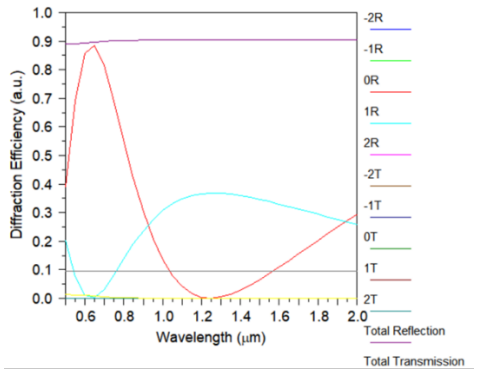
No tilt pixels, Non-linear phase level	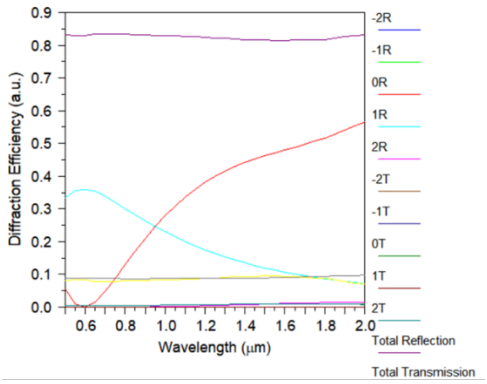	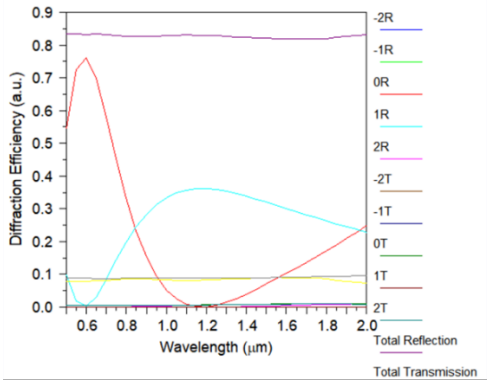

With tilt pixels, Non-linear phase level	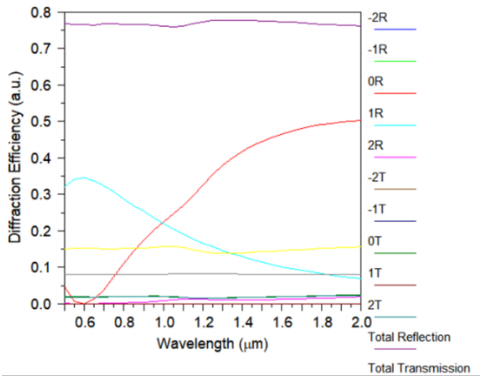	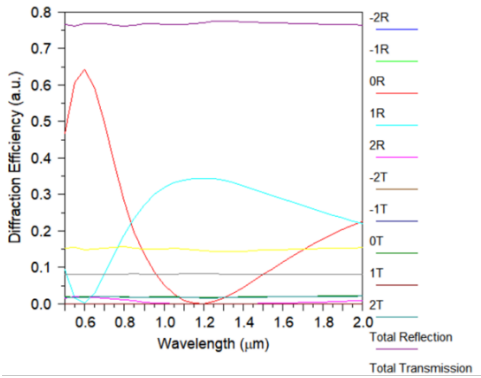

3.4 Experiment results and Analysis

In this experiment, we evaluated the diffraction efficiency of both single modulation and dual modulation at 532nm and 1550nm illuminations. 532nm measurements are used as a baseline data to be compared with the 1550nm results. Both blazed and binary gratings with various of grating periods are tested. Section 3.4.1 is the measurements from 532nm wavelength; section 3.4.2 is the main results of 1550nm illumination which confirmed our benefits from dual modulation at infrared wavelengths; last section contains a loss analysis of the dual modulation experiment tells us the threshold of the benefit wavelength.

3.4.1 532nm Comparison: Single Modulation vs Dual Modulation

In the 532nm diffraction efficiency evaluation experiment, the system schematic is shown in Fig. 3.19. Where collimating lenses and mirror with center hole are replaced with a beam splitter since our goal is to evaluate the loss and gain between single and dual modulation as while as between visible and infrared wavelength instead of to evaluate the total output from the system. This beam splitter can be used to separate the diffracted beam path from the incident beam path, and the 50% loss from the beam splitter can be neglect by calculate the diffraction efficiency with the incident

beam intensity that is normalized to the ratio of the beam splitter. In this setup, beam before the BS is already collimated, the mirror used for dual modulation is located on the top of a Piezo-actuated stage to adjust the pixel matching precisely, and camera (applied to confirm beam steering phenomenon occurs for dual modulation) is located after the microscope objective lens, which can be replaced with a Power meter detector.

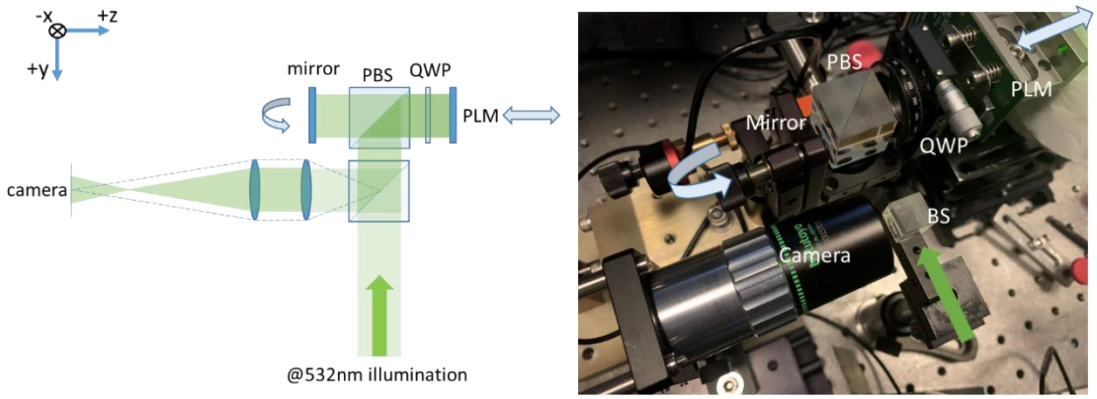

Figure 3.19 Schematic and setup diagram of 532nm diffraction efficiency evaluation experiment.

By adjusting the tip-tilt of the mirror, the pixel matching between the image of the PLM and PLM is adjusted where diffraction efficiency is also maximized since only perfect pixel matching can double the phase depth of single modulated PLM that optimize the diffraction efficiency. The PLM location is also being adjusted along the z direction to satisfy the Talbot distance requirement of dual modulation. The periodic variance of diffraction efficiency is observed when the PLM is slightly moving along the z-axis as well as mirror's tip-tilt is adjusted. Fig. 3.20 shows the relationship between the PLM position and diffraction efficiency, the results show that the peak of the diffraction efficiency roughly occurs at integer times of half Talbot distance both for 2 pixels/period and 4 pixels/period grating. Remember for the Talbot effect, we have conjugate phase reconstructions occur at 2 base distance that equals to half Talbot distance from the object

plane. At the conjugate phase reconstruction plane, with the mirror's tip-tilt is adjusted, the phase depth can also be perfect doubled results in a peak diffraction efficiency shown in Fig. 3.20.

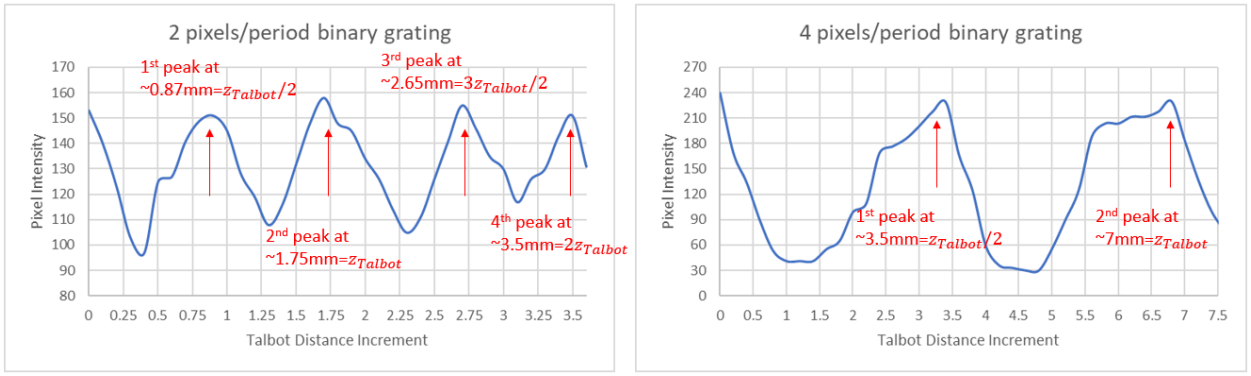

Figure 3.20 Relationship between the PLM location and diffraction efficiency with tip-tilt of mirror adjusted.

The diffraction efficiency (DE) measurement results of the single and dual modulation are depicted in Fig. 3.21. For the binary grating, DE of dual modulation is 20% less than the single modulation, and 30% less than the single modulation for blazed grating. This result agrees with the simulation in section 3.3.3 that dual modulation is relatively low at visible wavelength range for the PLM tuned for 633nm wavelength. These data can be used as a baseline data to be compared with the results in next section. During the experiment, we also observed relatively higher diffraction efficiency on the 2nd diffraction order for dual modulation at 532nm illumination. This also agrees with the simulation results that +/- 2nd order own a high DE for dual modulation at visible wavelength range.

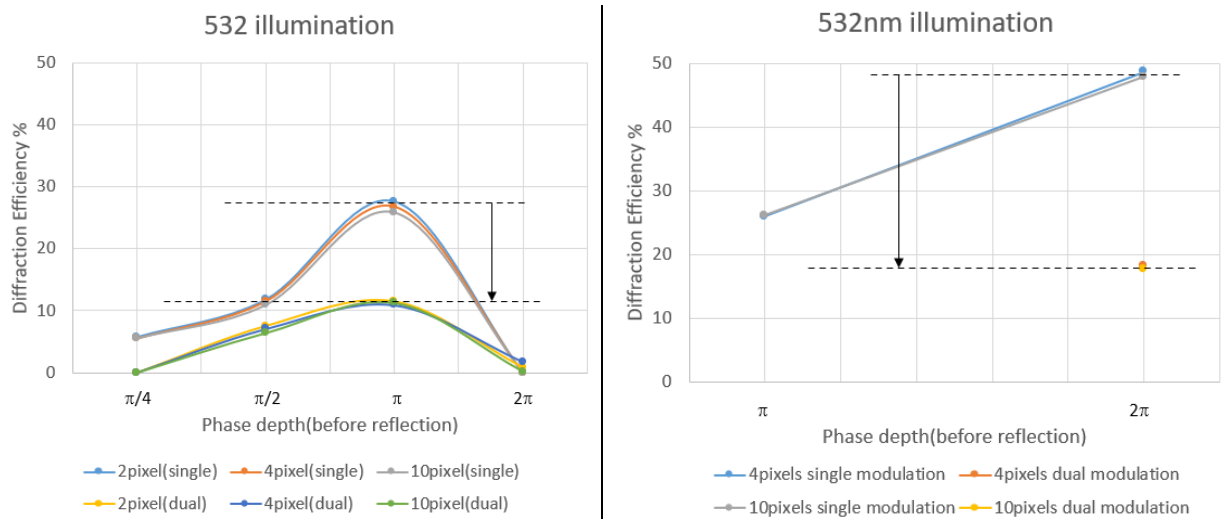

Figure 3.21 Baseline diffraction efficiency data of single modulation and dual modulation at 532nm wavelength. Left diagram is for various grating period binary grating with Phase modulation as horizontal axis; Right diagram is for blazed grating with grating period as the horizontal axis.

3.4.2 1550nm Comparison: Single Modulation vs Dual Modulation

Figure 3.22 shows the schematic of an optical setup for the dual modulation experiment at wavelength of 1550nm. The PBS, QWP, mirror, and focusing lens are replaced with components optimized at wavelength of 1550nm. A 1550nm laser source (Model LDC-3722B, ILX Lightwave) is collimated by a lens (Model F810APC, Thorlabs). The collimated 1550nm beam goes to the beam splitter and 1550nm detector (Model 8163A, Hewlett Packard) is used to measure the intensity of the diffracted beam. By rotating the QWP, the polarization of the beam is tuned so that we can switch between single and dual modulation without adjusting the whole system.

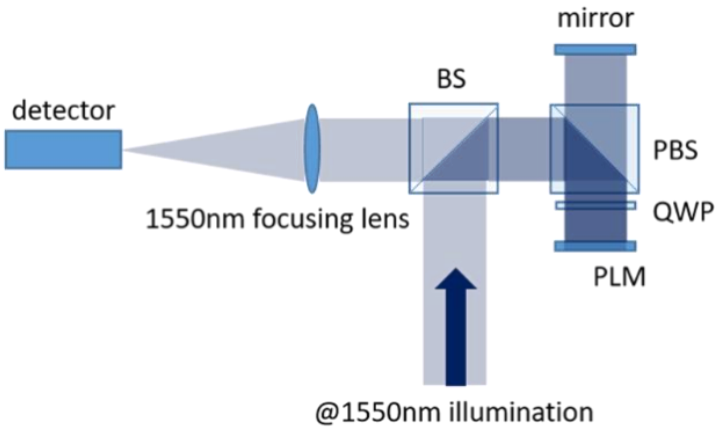

Figure 3.22 Schematic of 1550nm diffraction efficiency evaluation experiment.

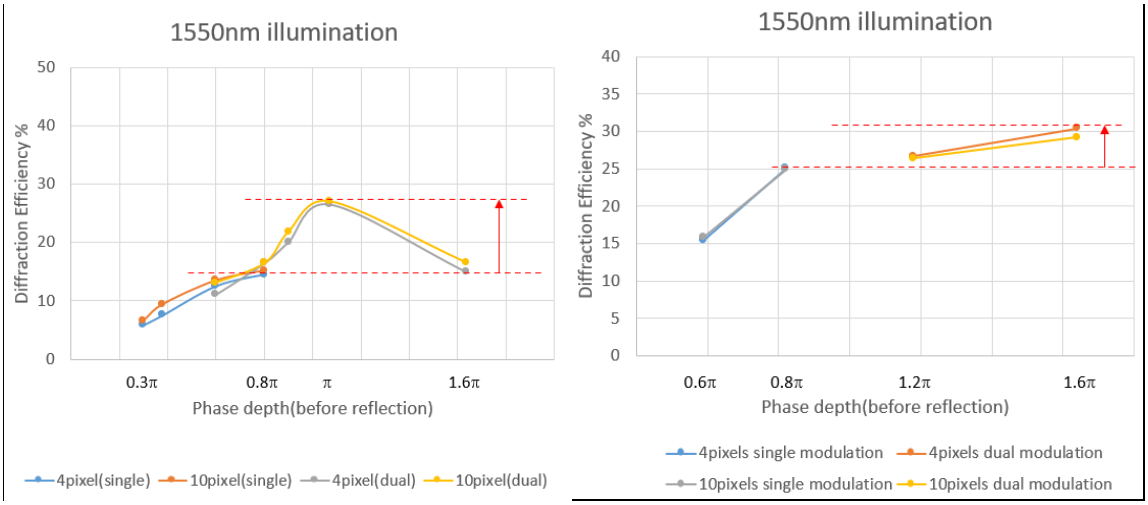

Figure 3.23 Diffraction efficiency results of single modulation and dual modulation at 1550nm wavelength. Left diagram is for various periods of binary grating with phase modulation as the horizontal axis; Right diagram is for various period of blazed grating with grating period as the horizontal axis.

Figure 3.23 depicts experimental result of dual phase modulation by using PLM designed for 2π phase modulation at 633nm. The maximum phase modulation with conventional single modulation is limited to:

$$\text{Maximum phase modulation} = 2\pi \times 633\text{nm}/\lambda \quad (9)$$

which is 0.8π for 1550nm. With the dual modulation, the phase modulation depth is doubled. Correspondingly, the diffraction efficiency increases from 20% with single modulation to 30% for dual modulation. The experimental results confirm feasibility of the proposed optical architecture that optically enhances phase modulation depth of reflective PLM at infrared wavelength range even the PLM is designed for visible wavelength.

3.4.3 Loss Analysis of Dual Modulation

In this experiment, in addition to the diffracted beam spots, we also observed bright spots from the Fresnel reflection of the PBS surfaces in the camera image. Optical components used in the system is anti-reflection coated for the wavelength of 532nm and 1550nm, there are still loss from each surfaces of optical components by Fresnel reflections. For the dual modulation, beam interacts with PLM twice. In addition, double path configuration increases loss from increased number of reflections of each surface. The loss from the surface reflection causes the decrease in diffraction efficiency as a total system, which limit enhancement of diffraction efficiency of dual modulation scheme.

Table 3.6 Calculation of 532nm surface reflection transmission and optical loss.

Components	Single modulation	Dual modulation
PBS	0.995	0.995
QWP	0.950	0.950
Al mirror	0.930	0.930
QWP	0.950	0.950
PBS	0.995	0.995
532nm High reflectivity mirror	NA	0.99
PBS	NA	0.995

QWP	NA	0.950
Al mirror	NA	0.93
QWP	NA	0.950
PBS	NA	0.995
Transmission	0.832	0.736
Optical Loss	0.182	0.338

Table 3.7 Experimental measurements result of 532nm surface reflectivity. PLM 0^{th} order single modulation reflectivity is measured in free space without optical components (meaning this is the net 0^{th} order diffraction efficiency), while dual modulation is measured with optical components depicted in Fig. 3.22 (counts twice 0^{th} order diffraction efficiency and once dual modulation system transmission).

		Single modulation	**Dual modulation**
Reflectivity	PLM (0^{th} order)	0.6698	0.3798
	Mirror	0.8515	0.7311
Difference of Loss between Single & Dual	PLM (0^{th} order)	0.29	
	Mirror	0.12	

Table 3.6 tabulates loss of single and dual modulation for 532nm experiment. The total transmission of the dual modulation is calculated to be 16% less than the transmission of the single modulation. Transmission of PLM is a measured efficiency of reflection from PLM with pixels are all flat as shown in Table 3.7. The value includes transmission of cover glass, reflectivity of Al coated micro mirror of PLM, fill factor of pixel and effect of random tilt of PLM pixels, where

single modulation 0^{th} DE is measures in free space (no optical components transmission) we call it net 0^{th} order DE (66.98% at 532nm), and net 0^{th} order DE in dual modulation is measured with optical components. This measured dual modulation 0th order diffraction efficiency 37.98% counts twice net 0th order diffraction efficiency and once dual modulation system transmission, which closely agrees with the calculated dual modulation 0th order diffraction efficiency: 66.98% (532nm net 0th order reflectivity for single path) ×66.98% (532nm net 0th order reflectivity for single path) ×73.70% ÷ (93%×93%) (1550nm dual modulation system transmission transmission without counting cover glass transmissions) = 38.23%. With a high reflectivity mirror that replace the PLM, the measurement results of system transmission (73.11%) agree well with the calculated result (73.70%). Remind the simulation in previous section, the diffraction efficiency goes up at infrared wavelength. The reflection loss from optical components as while as inaccurate system alignment will cause the dual modulation diffraction efficiency curve goes down.

Table 3.8 Calculation of 1550nm surface reflection transmission and optical loss.

Components	**Single modulation**	**Dual modulation**
PBS	0.995	0.995
QWP	0.98	0.98
Al mirror	0.97	0.97
QWP	0.98	0.98
PBS	0.995	0.995
Au mirror	NA	0.97
PBS	NA	0.995
QWP	NA	0.98
Al mirror	NA	0.97
QWP	NA	0.98
PBS	NA	0.995
Total Transmission	0.922	0.825

Optical Loss	0.077	0.174

Table 3.8 is a calculation of loss of single and dual modulation for 1550nm experiment. The total transmission of the dual modulation is calculated to be 10% less than the total transmission of the single modulation. Transmission of PLM is a measured efficiency of reflection from PLM with pixels are all flat as shown in Table 3.9. The value includes transmission of cover glass, reflectivity of PLM Al mirror, fill factor of pixel and effect of random tilt of PLM pixels, where single modulation 0th DE is measures in free space (no optical components transmission) we call it net 0th order DE (82.98% at 532nm), and dual modulation 0^{th} DE is measured with optical components. This measured dual modulation 0^{th} order diffraction efficiency counts twice net 0^{th} order diffraction efficiency and once dual modulation system transmission, which roughly agrees with the calculated dual modulation 0^{th} order diffraction efficiency: 82.98% (1550nm net 0^{th} order reflectivity for single path) ×82.98% (1550nm net 0^{th} order reflectivity for single path) ×82.51% ÷ (97%×97%) (1550nm dual modulation system transmission without counting cover glass transmissions) = 60.38%.

Table 3.9 Experimental measurements result of 1550nm surface reflectivity. PLM 0th order single modulation reflectivity is measured in free space without optical components (meaning this is the net 0th order diffraction efficiency), while dual modulation is measured with optical components (counts twice 0th order diffraction efficiency and once dual modulation system transmission).

		Single modulation	**Dual modulation**
Reflectivity	PLM (0^{th} order)	0.8298	0.5208

Difference of Loss between Single & Dual	PLM (0^{th} order)	0.309

Table 3.10 summarizes analysis of the critical wavelength (λ_c). The threshold wavelength is defined as a wavelength over which we benefit in terms of the diffraction efficiency by the dual modulation method. Simulation and experiment results of both single modulation and dual modulation are shown in this Table. The RCWA simulations only consider the nonlinear phase level into, i.e., no random tilt pixels, fill factor = 1, no cover glass transmission, and PLM's Al mirror reflectivity not included. In the simulation phase levels of CGH are optimized at each wavelength. Blue curve shows simulated diffraction efficiency of single modulation. Orange curve shows simulated diffraction efficiency of dual modulation. The experiment results of diffraction efficiency at 532nm and 1550nm are included in the plot from section 3.4, 4pixels and 10pixels period binary and blazed gratings. Green points are dual modulation experimental measurement result, and red points are from single modulation experimental results. Based on the loss analysis in this section, optical loss and wavelength dependent reflectivity is incorporated into the RCWA simulation results of dual and single modulation at 532 and 1550nm wavelength. At 1550nm illumination, we have a system transmission (does not include the PLM cover glass transmission) of 82.511% ÷ (97%×97%) = 87.6937% for dual modulation. In the dual modulation, we have beam that interacts with PLM twice. Also due to imperfection of PLM pixel array, such as random tilt micromirrors and gap between micromirrors, we expect that the light is diffracted to orders other than 0^{th} as Table 3.7 and 3.9 shows [14]. Therefore, the orange curve needs to be re-scaled by: Measured dual modulation system transmission (87.6937% for 1550nm, and 85.21% for 532nm) × Measured net 0^{th} order reflectivity of PLM (82.98% at 1550nm, and 66.98% at 532nm)

× Measured net 0^{th} order reflectivity of PLM = Re-scaling factor (60.383% for 1550nm, and 38.23% for 532nm). The yellow curve in Table 3.10 shows the dual modulation diffraction efficiency simulation that is adjusted by reflection loss from the system and from power spillover into diffraction orders not of interest, and gray curve shows the single modulation diffraction efficiency simulation that is re-scaled by: Measured single modulation system transmission (95.08% for 1550nm, and 89.47% for 532nm) × Measured net 0th order reflectivity of PLM (82.98% at 1550nm, and 66.98% at 532nm) = Re-scaling factor (78.90% for 1550nm, and 59.93% for 532nm).

Although re-scaling of RCWA simulation is feasible for 532nm and 1550nm for which measured 0^{th} order PLM reflectivity value is available, we need a model to predict diffraction efficiency over range of wavelength, 532 to 2000nm since the 0^{th} order diffraction efficiency depends on the wavelength. Therefore, we can back calculate the 0^{th} order diffraction efficiency for other wavelength based on the two points data we have at this point by using the Strehl Intensity Ratio (SIR) for PLM model, which is given by:

$$Strehl\ Radio = \frac{I_{aberrated}(0,0)}{I_{diffraction\ limited}(0,0)} \sim e^{-(k\sigma)^2} \quad (10)$$

, where σ^2 is the variance of wavefront error and k is the magnitude of propagation vector equals to $\frac{2\pi}{\lambda}$. The σ^2 represents variance of wave aberration due to imperfection of PLM pixel array, such as tilt and piston. Transmission of cover glass of PLM affects system efficiency too. The cover glass transmission is modelled as a monotonically decreasing linear function of wavelength, i.e., 100% at 532nm and 82% at 1550nm.

The calculated 0^{th} order reflectivity model for single and dual modulation at different wavelength are shown in Fig. 3.24 and are combined with the system transmission to calculate the re-scaling factor for the other wavelengths.

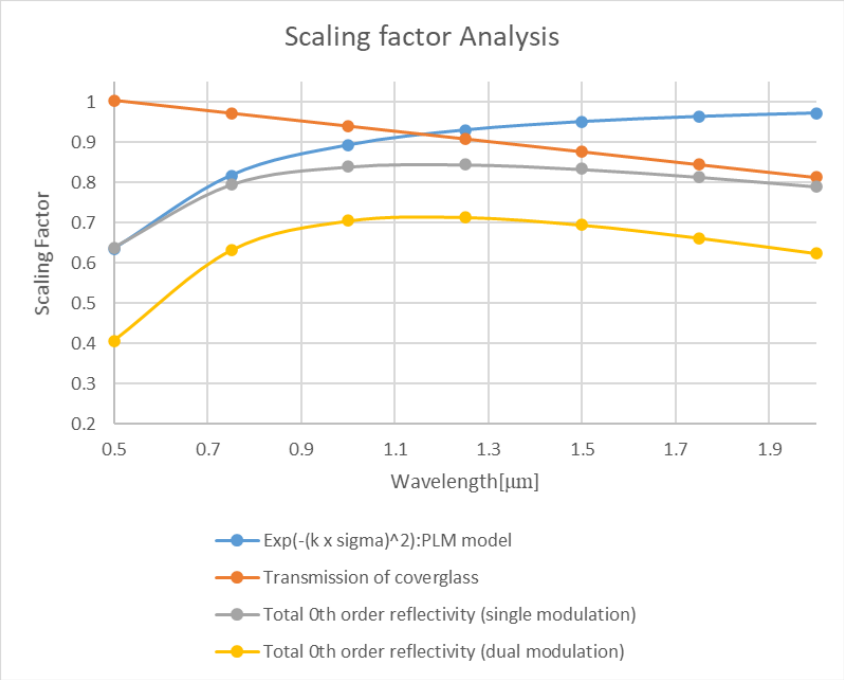

Figure 3.24 Scaling factor analysis result by using Strehl Intensity Radio.

Table 3.10 Dual modulation benefit wavelength threshold analysis of 4pixels period and 10pixels period binary and blazed gratings. Loss analysis based on no random tilt pixels, fill factor = 1, and nonlinear phase level simulations and optimized phase level for each wavelength.

	4 pixels per grating period	10 pixels per grating period

Binary Grating	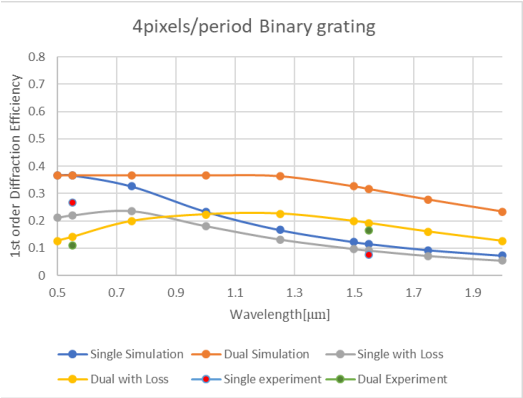	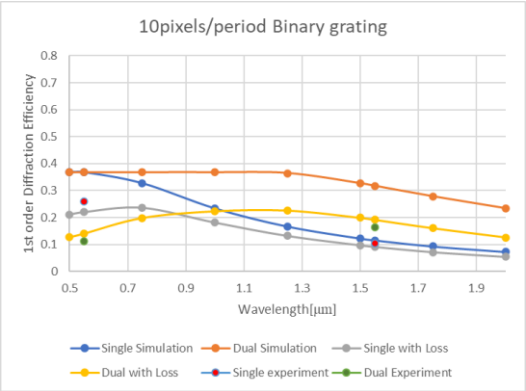
Blazed Grating	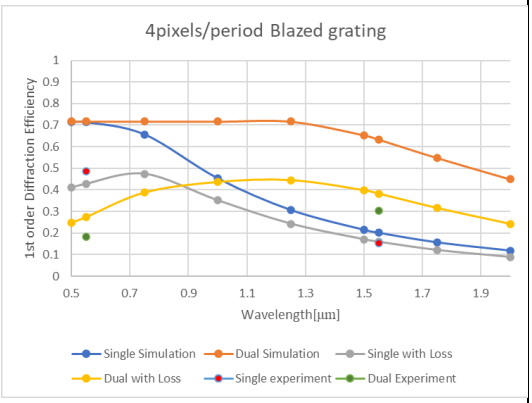	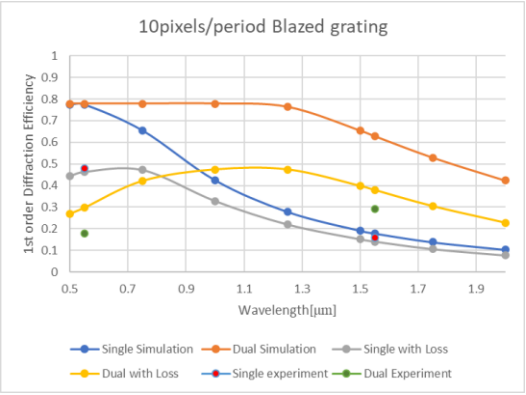

After rescaling the RCWA simulation results while taking the loss into account (gray and yellow curve in Table 3.10), the experimental results are well consistent to the simulation results. At 1550nm, the simulation shows that we still have 3%-10% gap to improve for the blazed grating. This would be because of a fact that system alignment for the blazed grating is more difficult compare to the binary grating. The crossing point between the gray curve and yellow curve shows the critical wavelength (λ_c) threshold above where the dual modulation method has an advantage in diffraction efficiency. Without taking the measured loss into account, λ_c is 0.6μm for an ideal PLM in use. With measured loss, λ_c is shifted about 0.3μm to longer wavelength or λ_c = 0.9μm. Based on the simulation, experiment, and loss analysis, at 1550nm wavelength, we have 2× more

improvement in diffraction efficiency between the single modulation (absolute DE single = 15%) and dual modulation (absolute DE dual = 30%) for blazed gratings. For binary grating, improvement factor is 2×, absolute DE single for single modulation = 10% and absolute DE dual for dual modulation = 20%. Compare all 4 figures, we can also conclude that gratings with more discrete phase levels perform better for dual modulation at longer wavelength, and blazed gratings perform better compare to binary gratings for dual modulation at longer wavelength. As we can see the critical wavelength for 10pixels/period blazed grating is 0.8μm instead of 0.9μm for other grating types. This consistent with the PLM diffraction efficiency equation (Eqn. 3), when me gets larger, 1st order diffraction efficiency increases.

The analysis shows 0th order reflectivity of PLM takes a critical role, which depends on several factors: cover glass transmission, fill factor, randomness of pixels tilt and piston, and reflectivity of Al micromirrors. Table 3.11 shows case study on how λ_c depends on degree of pixel tilt of micromirrors. We have assumed three cases on random tilt, a) +/-0.3deg, b) +/-0.15deg and c) +/-0deg for different types of gratings.

Table 3.11 Effect random tilt pixel on the critical wavelength analysis. Three cases on random tilt are assumed: a) +/-0.3deg, b) +/-0.15deg and c) +/-0deg. While fill factor = 1, cover glass transmission = 1, and reflectivity of Al micromirror = 1.

	4 pixels per grating period	10 pixels per grating period

Binary Grating	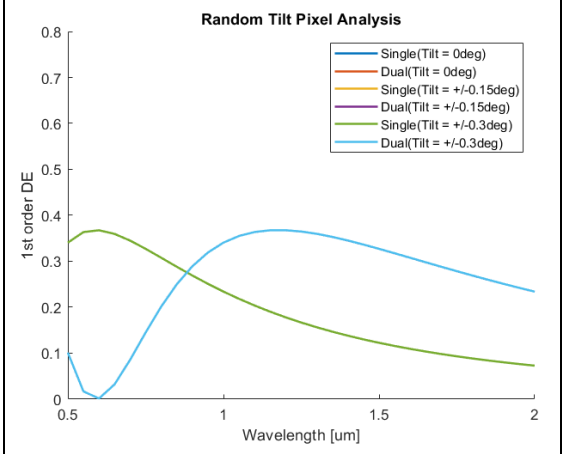	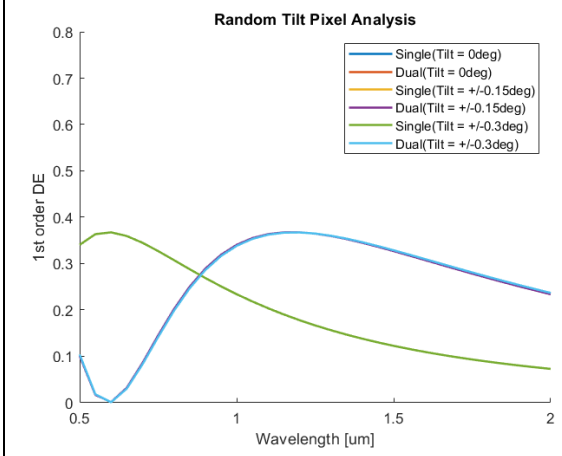
Blazed Grating	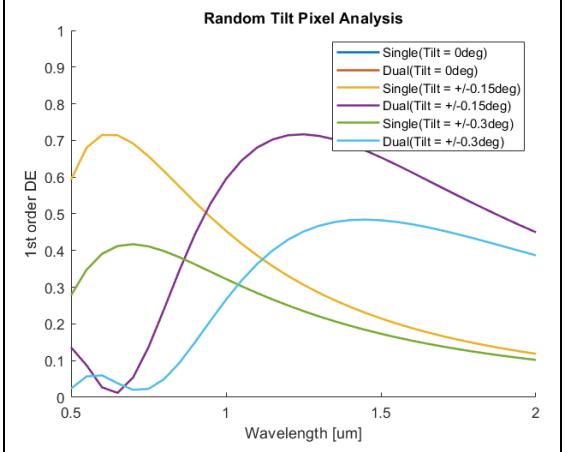	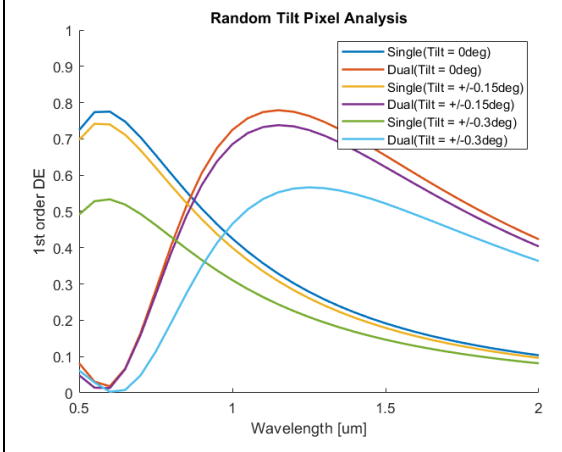

As depicted in Table 3.11 graphs. For 4 pixels period binary grating, the three cases are overlapped perfectly. For 10 pixels period binary grating, there is slightly offset between the curve of +/-0.3degree and 0degree. For 4 pixels period blazed grating, the offset between 0degree and +/-0.3degree become more significant. For 10 pixels period blazed grating, we observe offset between all three cases. This result means that the more discrete phase levels are more affected by the pixel tilt angle and that the blazed grating is more affected by the pixel tilt angle than the binary grating. Also, we observed the 4pixels/period blazed grating has the maximum amount of shift of the critical wavelength, which is shifted from 0.9μm to 1.05μm. The grating type is easier to be

affected by the pixel tilt angle than the discrete of the phase level, and tilt degree less than +/- 0.15degree not have too much effect on the critical wavelength.

3.5 Summary

In this chapter, we provide a method to optically enhance the diffraction efficiency for infrared beam steering of a 633nm designed PLM, which is doing dual modulation by using only one PLM. Both simulations, experimental results, and analysis are made. In the 532nm experiment, the dual modulation is less than the single modulation which agrees with the simulation results in section 3.3.3. While for 1550nm illumination, we benefit 2 times more in diffraction efficiency from the dual modulation compare to the single modulation. The critical wavelength is identified as 900 nm. This confirms the feasibility of diffraction efficiency enhancement for infrared beam steering applications by using device having a limited maximum phase modulation depth, for example 2π at 633nm.

Chapter 4. Conclusions

In this thesis, two main projects are reported. One is the stability evaluation of a Digital Micromirror Device based diffractive beam steering both from a long-term continuous operation perspective and heat cycling perspective. We confirmed that DMD based diffractive beam steering is stable over the time as expected. Also, the method of improve the stability by using a look-up table is also proposed. The second contribution is an optical enhancement of the diffraction efficiency of PLM designed for a 633nm, for longer wavelength applications. We proposed Talbot image-based enhancement of phase modulation depth of a Phase Light Modulators. We have confirmed that the proposed method enhances diffraction efficiency of PLM at 1550nm.

As an overall summary, core aspects of findings are re-described here.

In chapter 1, the working principle of DMD and PLM as while as the beam steering property of them are introduced, where DMD works as an amplitude spatial light modulator with diamond pixel array flipping between +/-12 degree around the diagonal line of each pixel and PLM works as a phase spatial light modulator with pixelated micromirrors array change the height along the direction of the surface normal. Some popular applications of such MEMS-based spatial modulation devices are also introduced at the end of chapter 1.

In chapter 2, the DMD based diffractive beam steering system was first continuously operated over 350 hours at 360Hz refresh rate of the micromirror. The diffraction efficiency remains high during the whole process. After the 350 hours, the system is still operating in the Lab, the data not included in this thesis but shows high stability over months at room temperature without heatsink attached to the system. The second part is a heat cycling test, where the DMD micromirror surface was heated up to 75 C degree and back to the 45 C degree in 5 hours. During this process, the diffraction

efficiency decreased and went to the lowest at the highest temperature. This shows relatively low stability of the system when change temperature, which can be solved by programming the delay of the synchronization between the laser pulse and micromirror flipping.

In chapter 3, a newly proposed method named dual modulation is proposed to optically enhance the diffraction efficiency for a PLM based beam steering system for infrared applications. As mentioned in chapter 3, when use PLM deigned at visible wavelength for the infrared wavelength, the maximum phase depth will decrease since infrared wavelength is large compare to visible wavelength. If single modulated PLM is used optically twice, not using two physical PLMs, then we can double the phase depth which gives us higher diffraction efficiency for longer wavelength applications without modifying the PLM. In this experiment, the results show benefit wavelength of diffraction efficiency for dual modulation is at 1μm, and we have 2× improvement in the dual modulation diffraction efficiency compare to the single modulation for both blazed gratings and binary gratings. The experimental results combined with the simulation results and loss analysis confirmed that the dual modulation performs much better at longer wavelength compare to single modulation.

APPENDIX A – PUBLICATIONS, PATENT, AND FUNDING

Publications

[1] Jiafan Guan, Erik Evans, Heejoo Choi, and Yuzuru Takashima "Stability of diffractive beam steering by a digital micromirror device", Proc. SPIE 11698, Emerging Digital Micromirror Device Based Systems and Applications XIII, 116980I (5 March 2021); https://doi.org/10.1117/12.2582899

[2] Diffraction Efficiency Enhancement of PLM for Infrared Beam Steering. [To be submitted]

Invention disclosure

[3] Patent Disclosure UA21-201 Optical Enhancement of Phase Modulation Depth for a Phase Light Modulator

Report

[4] SRC Task #2810.053 TI PLM to Advanced Lidar and Display Systems

Funding

SRC Task #2810.053 TI PLM to Advanced Lidar and Display Systems

APPENDIX B – ARDUINO CODE FOR DMD BEAM STEERING

Main code:

```
#include "arduino2.h" // include the fast I/O 2 functions
#include <SPI.h>
// The I/O 2 functions use special data type for pin
// Definitions for SPI library:
// * Pin 11 = MOSI (Master Out Slave In) = D_In
// * Pin 12 = MISO (Master In Slave Out) = D_Out
// * Pin 13 = SCLK

#define NOP __asm__ __volatile__ ("nop\n\t")    //define NOP

const GPIO_pin_t Laser_Out = DP9;   // Laser output pin (or input into DS1023, currently omitted)
const GPIO_pin_t DMD_trigger = DP8; //Trigger signal for DMD

#define N_Orders 10
#define N_Slow 100
#define Laser_Speed_Limiter 5000   // Slows down laser pulsing

void setup() {
  pinMode2f(DMD_trigger, OUTPUT);
  digitalWrite2f(DMD_trigger, LOW);

  pinMode2f(Laser_Out, OUTPUT);
  digitalWrite2f(Laser_Out, LOW);

  pinMode2f(DMD_trigger, OUTPUT);
```

```
  digitalWrite2f(DMD_trigger, LOW);

  delay(3000);

  noInterrupts();
}

void loop() {
  int order = 0;
  int NumNOP = 0;
  int microsec = 0;
  int n_slow = 0;

  //  int Delay1023 = 0;

  while (1) {
    for (order = 0; order < N_Orders; order++) {
      switch (order) {
        case (0):
          NumNOP = 7;
          //         Delay1023 = 20;
          microsec = 377;
          break;
        case (1):
          NumNOP = 19;
          //         Delay1023 = 20;
          microsec = 377;
          break;
```

```
case (2):
  NumNOP = 29;
  //        Delay1023 = 23;
  microsec = 377;
  break;
case (3):
  NumNOP = 36;
  //        Delay1023 = 52;
  microsec = 377;
  break;
case (4):
  NumNOP = 42;
  //        Delay1023 = 104;
  microsec = 377;
  break;
case (5):
  NumNOP = 58;
  //        Delay1023 = 22;
  microsec = 377;
  break;
case (6):
  NumNOP = 70;
  //        Delay1023 = 22;
  microsec = 377;
  break;
case (7):
  NumNOP = 80;
  //        Delay1023 = 20;
```

```
    microsec = 377;
    break;
  case (8):
    NumNOP = 87;
    //        Delay1023 = 20;
    microsec = 377;
    break;
  case (9):
    NumNOP = 93;
    //        Delay1023 = 20;
    microsec = 377;
    break;
} // end order switch

for (n_slow = 0; n_slow < N_Slow; n_slow++) {
  digitalWrite2f(DMD_trigger, HIGH);  //Start DMD to begin transition.
  delayMicroseconds(microsec);       //Wait 218us for DMD to begin transitioning.
  delayNOP(NumNOP);                  //Coarse delay of number of NOPs
  NOP;
  digitalWrite2f(Laser_Out, HIGH);    //Send laser pulse (DS1023 currently omitted)
  NOP;
  digitalWrite2f(Laser_Out, LOW);
  delayMicroseconds(200);
  digitalWrite2f(DMD_trigger, LOW);
  // Reset DMD back to black
  delay(1);
  digitalWrite2f(DMD_trigger, HIGH); //Switch DMD2 back to original position
  delayMicroseconds(200);
```

```
      digitalWrite2f(DMD_trigger, LOW);
      delayMicroseconds(200);

//       delayMicroseconds(Laser_Speed_Limiter);
     } // End slow
   } // End order for loop
  }// end while loop
}// end void loop

void delayNOP(int DelayNOP) {
  switch (DelayNOP) { //switch statement delays at increments of 62.5ns
  Add 128 case of NOP for delay.
  } //END SWITCH-CASE STATEMENT
}
```

APPENDIX C – MATLAB CODE FOR PLM CGH GENERATION

Main code:

```
%% Unslanted phase grating for different grating period
close all;clear all;clc
Hrange = 0.0493*2;
period_mode = 8; % grating period

switch period_mode
    case 2
        Vrange = 1.7027;
    case 3
        Vrange = 1.119;
    case 4
        Vrange = 0.8819;
    case 8
        Vrange = 0.5531;
    case 10
        Vrange = 0.4841;
end

NH = 1;
NV = 1;
x = linspace(-Hrange/2, Hrange/2, NH);

if NV == 1
    y = Vrange;
    else
    y = linspace(-0.002, Vrange/2, NV+1);
    y = y(1:NV+1);
end

[xa, ya] = meshgrid(x, y);
theta = atan(sqrt(xa.^2+ya.^2));
phi = (xa>=0).*atan(ya./xa) + (xa<0).*(atan(ya./xa)+sign(ya)*pi);


for i = 1 : NH
    for j = 1: NV
        BiGRT = Grating_function(theta(j,i), phi(j,i));
        s = i+(j-1)*NH;

        %%%%%%%%%%%%%%%%%%%%
        gamma = 0.5;
        FTGRT = (abs(fftshift(fft2(ifftshift(BiGRT))))).^gamma;
        %%%%%%%%%%%%%%%%%%%%

        if s < 10
```

```
            imwrite(mat2gray(BiGRT),
sprintf('./blazedphase/grt_0%d.bmp', s));
            %%%%%%%%%%%%%%%%%%%%
            imwrite(mat2gray(FTGRT),
sprintf('./blazedphase/FTgrt_0%d.bmp', s));
            %%%%%%%%%%%%%%%%%%%%
        else
            imwrite(mat2gray(BiGRT),
sprintf('./blazedphase/grt_%d.bmp', s));
            %%%%%%%%%%%%%%%%%%%%
            imwrite(mat2gray(FTGRT),
sprintf('./blazedphase/FTgrt_0%d.bmp', s));
            %%%%%%%%%%%%%%%%%%%%
        end
    end
end
```

Function code:

```
function BiGRT = Grating_function(theta, phi)

nx = 0; % PLM surface normal
ny = 0;
nz = 1;
kx = sin(theta)*cos(phi);
ky = sin(theta)*sin(phi);
kz = cos(theta);
lbd = 532e-9; % wavelength of laser
k0 = 2*pi/lbd;

pw = @(x, y, z) exp(1j*k0*((kx-nx)*x+(ky-ny)*y+(kz-nz)*z)); % Plane
wave

% PLM parameters
pp = 10.8e-6;
h = 960;
v = 540;

w = (1:h)*pp;
h = (1:v)*pp;

[U, V] = meshgrid(w, h);

grating_mode = 1 ;% 0:horizontal grating; 1:vertival grating
step_mode = 8; % grating period
switch grating_mode
    case 0
        BiGRT = angle(pw(0, V, 0)); % Phase grating
    case 1
        BiGRT = angle(pw(U, 0, 0));
end
```

```
% BiGRT = (BiGRT <= 0); % Binary amplitude grating
p_0 = [0 0;1 1];
p_1 = [0 0;0 1];
p_2 = [0 0;0 0];
p_3 = [1 0;1 1];
p_4 = [0 0;1 0];
p_5 = [1 0;0 1];
p_6 = [1 0;1 0];
p_7 = [1 0;0 0];
p_8 = [0 1;1 1];
p_9 = [0 1;0 1];
p_10 = [0 1;1 0];
p_11 = [0 1;0 0];
p_12 = [1 1;1 1];
p_13 = [1 1;0 1];
p_14 = [1 1;1 0];
p_15 = [1 1;0 0];
%% binary phase mapping

switch step_mode

    case 10

GRT = cell(960,540);
[r,c] = size(BiGRT);

%%10_pixel blazed case with no round_ceil_floor function:
for o = 1:r
    for k = 1:c
        p = BiGRT(o,k);
        if  p <= -0.5 & p >= -1.1
            p = p_0;
            GRT{o,k} = p;
        elseif   p > -1.7 & p <= -1.2
            p = p_0;
            GRT{o,k} = p;
        elseif   p > -2.3 & p <= -1.75
            p = p_0;
            GRT{o,k} = p;
        elseif p > -2.9 & p <= -2.5
            p = p_0;
            GRT{o,k} = p;
        elseif   p > 2.7
            p = p_0;
            GRT{o,k} = p;
        elseif p > 2.1 & p <= 2.6
            p = p_8;
            GRT{o,k} = p;
        elseif  p > 1.5 & p <= 2
            p = p_8;
            GRT{o,k} = p;
        elseif p > 0.8 & p<=1.3
```

```
            p = p_8;
            GRT{o,k} = p;
        elseif p > 0.2 & p <= 0.7
            p = p_8;
            GRT{o,k} = p;
        elseif p >= -0.4 & p<=0
            p = p_8;
            GRT{o,k} = p;
        end
    end
end
BiGRT = cell2mat(GRT);

    case 8

GRT = cell(960,540);
[r,c] = size(BiGRT);

%%8_pixel blazed case with no round_ceil_floor function:
for o = 1:r
    for k = 1:c
        p = BiGRT(o,k);
        if  p <=-2
            p = p_0;
            GRT{o,k} = p;
        elseif   p > -2 & p <= -1.5
            p = p_7;
            GRT{o,k} = p;
        elseif   p > -1.5 & p <= -0.5
            p = p_11;
            GRT{o,k} = p;
        elseif p > -0.5 & p <= 0.5
            p = p_15;
            GRT{o,k} = p;
        elseif   p > 0.5 & p<= 1
            p = p_0;
            GRT{o,k} = p;
        elseif p > 1 & p <= 2
            p = p_7;
            GRT{o,k} = p;
        elseif  p > 2 & p <= 2.5
            p = p_11;
            GRT{o,k} = p;
        elseif p > 3
            p = p_15;
            GRT{o,k} = p;
        end
    end
end
BiGRT = cell2mat(GRT);

    case 4
```

```
%4_level blazed case;
GRT = cell(960,540);
[r c] = size(BiGRT);

for o = 1:r
    for k = 1:c
        p = BiGRT(o,k);
        if p >= -2.2 & p <=-1.5
            p = p_0;
            GRT{o,k} = p;
        elseif p >= 2.5 & p <= 3.3
            p = p_0;
            GRT{o,k} = p;
        elseif p > 1 & p <= 1.7
            p = p_11;
            GRT{o,k} = p;
        elseif p > -0.5 & p <= 0
            p = p_11;
            GRT{o,k} = p;
        end
    end
end
BiGRT = cell2mat(GRT);

    case 3
%3_level blazed case;
GRT = cell(960,540);
[r c] = size(BiGRT);

for o = 1:r
    for k = 1:c
        p = BiGRT(o,k);
        if p >= -3 & p <=-2
            p = p_0;
            GRT{o,k} = p;
        elseif p >= 1 & p <= 2.5
            p = p_8;
            GRT{o,k} = p;
        elseif p > -1 & p <= 0
            p = p_11;
            GRT{o,k} = p;
        end
    end
end
BiGRT = cell2mat(GRT);

    case 2
%binary grating;
GRT = cell(960,540);
[r c] = size(BiGRT);

for o = 1:r
```

```
    for k = 1:c
        p = BiGRT(o,k);
        if p >= 1.5 & p <= 3.5
            p = p_0;
            GRT{o,k} = p;
        elseif p >= -1.5 & p <= 0
            p = p_11;
            GRT{o,k} = p;
        end
    end
end
BiGRT = cell2mat(GRT);

End
```

REFERENCES

[1] Hans Dieter Tholl, "Novel laser beam steering techniques," Proc. SPIE 6397, Technologies for Optical Countermeasures III, 639708 (5 October 2006); https://doi.org/10.1117/12.689900

[2] "DLP7000 DLP® 0.7 XGA 2x LVDS Type A DMD", Texas Instruments, Literature Number: DLPS026F –AUGUST 2012–REVISED JUNE 2019

[3] Smith, B., Hellman, B., Gin, A., Espinoza, A., and Takashima, Y., "Single chip lidar with discrete beam steering by digital micromirror device," Opt. Express 25, 14732–14745 (Jun 2017).

[4] Joshua Rodriguez, Braden Smith, Eunmo Kang, Brandon Hellman, Guanghao Chen, Adley Gin, Alonzo Espinoza, and Yuzuru Takashima "Beam steering by digital micro-mirror device for multi-beam and single-chip lidar", Proc. SPIE 10757, Optical Data Storage 2018: Industrial Optical Devices and Systems, 107570F (14 September 2018); doi: 10.1117/12.2323757; https://doi.org/10.1117/12.2323757

[5] Yajun Wang, Bhaskar Bhattacharya, Eliot H. Winer, Peter Kosmicki, Wissam H. El-Ratal, Song Zhang, Digital micromirror transient response influence on superfast 3D shape measurement, Optics and Lasers in Engineering, Volume 58, 2014, Pages 19-26, ISSN 0143-8166,https://doi.org/10.1016/j.optlaseng.2014.01.015.(https://www.sciencedirect.com/science/article/pii/S0143816614000165)

[6] "TI DLP® LightCrafter™ 4500 Evaluation Module User's Guide", Texas Instruments, Literature Number: DLPU011F July 2013–Revised July 2017

[7] Sontheimer, A.B.. (2002). Digital Micromirror Device (DMD) hinge memory lifetime reliability modeling. 118 - 121. 10.1109/RELPHY.2002.996622.

[8] Douglass, Michael. (2003). DMD reliability: a MEMS success story. Proceedings of SPIE - The International Society for Optical Engineering. 4980. 10.1117/12.478212.

[9] Dudley, Dana & Duncan, Walter & Slaughter, John. (2003). Emerging Digital Micromirror Device (DMD) Applications. Proceedings of SPIE - The International Society for Optical Engineering. 4985. 10.1117/12.480761.

[10] Raymond K. Kostuk. Holography Principles and Applications. International Standard Book Number-13: 978-1-4398-5583-6 (Hardback)

[11] Tom D. Milster. OPTI505R Handbook Chapter 5 Scalar Diffraction.

[12] Yuzuru Takashima and Brandon Hellman, "Review paper: imaging Lidar by Digital Micromirror Device", Special Section: Invited Review Paper, Optical Review (Sep. 6, 2020).DOI: 10.1007/s10043-020-00620-w

[13] Joseph W. Goodman. Introduction to Fourier Optics [4th edition]. Library of Congress Control Number: 2017930862. ISBN 978-1-319-15304-5 (epub) © 2017 by W. H. Freeman and Company

[14] Terry A. Bartlett, William C. McDonald, and James N. Hall "Adapting Texas Instruments DLP technology to demonstrate a phase spatial light modulator", Proc. SPIE 10932, Emerging Digital Micromirror Device Based Systems and Applications XI, 109320S (4 March 2019); https://doi.org/10.1117/12.2514483

[15] Jiafan Guan, Erik Evans, Heejoo Choi, and Yuzuru Takashima "Stability of diffractive beam steering by a digital micromirror device", Proc. SPIE 11698, Emerging Digital Micromirror Device Based Systems and Applications XIII, 116980I (5 March 2021); https://doi.org/10.1117/12.2582899